



This is a repository copy of *3D ISPH Erosion Model for Flow Passing a Vertical Cylinder*.

White Rose Research Online URL for this paper:  
<http://eprints.whiterose.ac.uk/125864/>

Version: Accepted Version

---

**Article:**

Wang, D., Shao, S., Li, S. et al. (3 more authors) (2018) 3D ISPH Erosion Model for Flow Passing a Vertical Cylinder. *Journal of Fluids and Structures*, 78. pp. 374-399. ISSN 0889-9746

<https://doi.org/10.1016/j.jfluidstructs.2018.01.003>

---

**Reuse**

This article is distributed under the terms of the Creative Commons Attribution-NonCommercial-NoDerivs (CC BY-NC-ND) licence. This licence only allows you to download this work and share it with others as long as you credit the authors, but you can't change the article in any way or use it commercially. More information and the full terms of the licence here: <https://creativecommons.org/licenses/>

**Takedown**

If you consider content in White Rose Research Online to be in breach of UK law, please notify us by emailing [eprints@whiterose.ac.uk](mailto:eprints@whiterose.ac.uk) including the URL of the record and the reason for the withdrawal request.



[eprints@whiterose.ac.uk](mailto:eprints@whiterose.ac.uk)  
<https://eprints.whiterose.ac.uk/>

# 3D ISPH Erosion Model for Flow Passing a Vertical Cylinder

Dong Wang<sup>1,2</sup>, Songdong Shao<sup>3</sup>, Shaowu Li<sup>1,\*</sup>, Yang Shi<sup>1</sup>, Taro Arikawa<sup>4</sup>, Hongqian Zhang<sup>1</sup>

<sup>1</sup> State Key Laboratory of Hydraulic Engineering Simulation and Safety, Tianjin University, Tianjin 300072, China

Email: [lishaowu@tju.edu.cn](mailto:lishaowu@tju.edu.cn); [shiyang@tju.edu.cn](mailto:shiyang@tju.edu.cn); [zhanghongqian\\_tju@163.com](mailto:zhanghongqian_tju@163.com)

<sup>2</sup> Department of Civil & Environmental Engineering, National University of Singapore, 21 Lower Kent Ridge Road, Singapore 119077

Email: [ceewadg@nus.edu.sg](mailto:ceewadg@nus.edu.sg)

<sup>3</sup> Department of Civil and Structural Engineering, University of Sheffield, Sheffield S1 3JD, United Kingdom

Email: [s.shao@sheffield.ac.uk](mailto:s.shao@sheffield.ac.uk)

<sup>4</sup> Coastal Engineering Laboratory, Civil and Environmental Engineering, Faculty of Science and Engineering, Chuo University, 1-13-27 Kasuga, Bunkyo-ku, Tokyo, Japan

Email: [arikawa@civil.chuo-u.ac.jp](mailto:arikawa@civil.chuo-u.ac.jp)

\* Author of correspondence, Email: [lishaowu@tju.edu.cn](mailto:lishaowu@tju.edu.cn)

## Abstract

In this paper a 3D incompressible Smoothed Particle Hydrodynamics (ISPH) erosion model is proposed to simulate the scouring process behind a large vertical cylinder. The erosion model is based on the turbidity water particle concept and the sediment motion is initiated when the fluid bottom shear stress exceeds the critical value. The previous 2D SPH sediment initiation model is expanded by combining the effects of both transverse and longitudinal sloping beds in a practical 3D situation. To validate the developed model, a laboratory flume experiment was carried out to study the clear water scouring around a vertical cylinder under unidirectional current, in which high-speed video cameras were used for the real-time monitoring of sediment movement. The 3D ISPH results are compared with the experimental data with good agreement in terms of the scouring patterns and scales. Besides, the computed flow velocity field suggests that both the horseshoe vortices and lee-wake flows around the cylinder have been accurately simulated.

**Keywords:** 3D ISPH; erosion model; large vertical cylinder; turbidity water particle; shear stress

## 1. Introduction

The non-cohesive sediment bed scouring initiated by the existence of a submerged structure is a popular topic widely investigated in both the fluvial and offshore environment. Dealing with the safety assessment of a structure placed on the riverbed (e.g. bridges, barrages etc.), the erosive action of the river stream must be reliably evaluated (Dordoni et al., 2010; Guandalini et al., 2012). Also, in the design of highly demanding marine structures, the scour around the foundations should be carefully considered (Petrini et al., 2010). Quite a few empirical formulas to predict the final scouring are available, but the phenomenon is time-dependent and it is affected by several uncertainties related to both the sediment and the flow characteristics. Most predictive formulas for scouring behind a vertical cylinder under either current or wave condition are established from the experimental observations on relatively small size of the cylinder. Using these formulas for field applications could suffer large error if the large cylinder diameters are encountered. Ettema et al. (2006) found that the intensity and frequency of vortices generated during a large cylinder scouring are much smaller than those generated during a smaller cylinder. Moreover, due to the differences in experimental conditions, there exist substantial divergences of the result among various empirical predictive methods. Early numerical studies in this field are attributed to Olsen and Melaaen (1993), Richardson and Panchan (1998), Olsen and Kjellesvig (1998) and Roulund et al. (2005), in which only a small cylinder was used. Although Sheppard et al. (2004) investigated a large pier scouring with diameter of 0.914 m, the dynamic vortex evolutions were not observed. Generally speaking, there are plenty of documented works on the final size and shape during the cylinder scour, but there is limited information on the dynamic process.

The Smoothed Particle Hydrodynamics (SPH) method emerged as a promising tool for free surface flow simulations, which involve large deformation of water surface and multi-phase interface. Compared with its popular applications in the coastal hydrodynamics, the SPH's versatility in simulating 3D sediment scouring behind a vertical cylinder has not been thoroughly explored. Most SPH works simply treated the cylinder as a 2D configuration in order to save computational expenses. For example, Morris et al. (1997) carried out a pioneering SPH study on low Reynolds number flows passing a regular lattice of the cylinders and compared the results with finite element solutions. Yildiz et al. (2009) improved the SPH solid boundary treatment by using a multiple boundary tangent approach and studied the flow interactions with an obstacle with complex curved boundaries. Ellero and Adams (2011) considered very viscous flow of the Newtonian liquid passing through a linear array of the cylinders confined in a channel and disclosed the mixing of shear and extensional behaviors. Omidvar et al. (2012) developed a variable mass SPH to investigate water waves generated by a heaving cylinder and water wave scattering by a fixed cylinder. Marrone et al. (2013) adopted a ghost-fluid technique, which led to a more accurate enforcement of the solid boundary. Their model was used to study the evolution of a viscous

flow around a blunt body for different Reynolds numbers. Nestor and Quinlan (2013) presented a Finite Volume Particle approach using the pressure projection for fully incompressible flow interacting with a rigid body. The developed model was applied to the Vortex-Induced Vibration (VIV) of a circular cylinder in laminar cross-flow. By adopting a parallel SPH model, Wen et al. (2016) proposed 3D numerical wave basin to study the wave impact on a vertical cylinder. Their OpenMP programming technology, combined with an existing MPI program contained in the parallel version of SPHysics code, was implemented to enable the simulation of several hundred million particles. The latest work in this field was reported by Bouscasse et al. (2017) for viscous flow past a circular cylinder interacting with free surface under varying cylinder submergences and Froude numbers. Besides, quite a few new progresses have been reported in the improvement of ISPH numerical schemes, such as the high accuracy first-order derivative calculation (Zheng et al., 2017), the optimized particle regularization (Khayyer et al., 2017a), the energy conservation of project-based particle methods (Khayyer et al., 2017b) and the enhanced two-step semi-implicit pressure solution (Xu and Lin, 2017).

On the other hand, some good progresses have also been made in the SPH modeling of sediment flows. Zanganeh et al. (2012) incorporated a soft contact approach to simulate the inter-particle collisions by a two-phase Lagrangian coupling model and studied the scouring beneath a marine pipeline, where the fluid and sediment phases were respectively modeled as Newtonian and non-Newtonian fluids, respectively. Ran et al. (2015) developed an ISPH sediment erosion model based on the concept of pick-up flow velocity, in which the sediment was initiated when the local flow velocity exceeded the critical value. This model was used to the movable bed scour and sediment grain movement under a dam break. Fu and Jin (2016) treated the sediment motion as multiphase flow and they developed a particle-based rheological model with higher-order viscosity smoothing scheme for the open channel flow scouring and water-sediment dam break flow. Fourtakas and Rogers (2016) proposed an SPH scheme by treating the liquid-sediment phases using the Newtonian and non-Newtonian Bingham-type constitutive model. This was further strengthened with the Drucker-Prager yield criterion to predict onset motion of the sediment grains. Khanpour et al. (2016) developed a two-phase SPH model in which both the water and sediment materials were treated as continuum to follow the governing equations of motion. They successfully reproduced the sediment scouring and deposition areas for a wall-jet and the sediment failure slopes for a flushing case. The model principle was that both the Mohr-Coulomb and the Shields yielding criteria were combined to determine the critical shear stress, above which the sediment materials start to behave like a viscous fluid. In a more recent study, Pahar and Dhar (2017) developed a robust multi-phase ISPH model further including the particle contact mechanism to account for the interactions between the water and sediment and the relevant drag forces. On the other hand, an early pioneering review on the multi-phase particle modeling techniques has been made by Gotoh and Sakai (2006).

In terms of existing SPH practice to model the sediment scouring, there are two different

approaches: (1) Most of documented works treated the water and sediment as different fluid components and therefore, relevant interaction models are used to link the two phases (Shakibaeinia and Jin, 2011; Manenti et al., 2016); (2) The other approach, which will also be adopted in the present paper, considered the counterbalance between the fluid force and sediment bed resistance. As a result, either the critical velocity (Hayashi et al., 2003; Ran et al. 2005) or the critical shear stress (Manenti et al., 2012) criterion can be used to determine the initiation of sediment particles when the threshold condition is satisfied. The purpose of present research is to develop a 3D ISPH sediment erosion model to study movable bed scours around a vertical circular cylinder. The model is a significant expansion of the previous 2D Turbidity Water Particle approach (Wang et al., 2016) by further including the sediment initiation model in both longitudinal and transverse directions. For the validation, laboratory flume experiment was carried out in Tianjing University, where detailed real-time dynamic scouring processes were recorded on multi-locations of the observation area. The cylinder diameter used in the experiment was 60 cm, and this reaches a reasonable scale to approximate the practical situation. In this work an incompressible SPH (ISPH) numerical scheme is adopted. One important advantage of the ISPH over the standard weakly compressible SPH is the accurate flow field computation. The ISPH can obtain the noise-free particle distribution, velocity and pressure patterns without any additional numerical smoothing techniques, such as the XSPH or density filtering widely used in the standard WCSPH. For the proposed study of flow passing around a vertical cylinder and associated sediment bed scouring, the relevant physical process should be very sensitive to the computed flow velocity and pressure field near the cylinder. Therefore the ISPH model could be expected to provide a better representation of the physical reality.

The present paper is structured as follows: section 2 is the development of 3D ISPH sediment erosion model and relevant numerical treatment; section 3 is the model validation by benchmark data on flow field over a fixed cylinder bed; section 4 introduces the laboratory experiment of movable bed scour and measurement; section 5 is dedicated to the SPH model application and validation by using the observed laboratory data, as well as the discussions on the flow-cylinder interaction and scour development over a movable bed; and section 6 concludes the whole work.

## **2. 3D ISPH Erosion Model**

### **2.1 3D ISPH fluids solver**

The present ISPH fluids model is based on the state-of-art numerical scheme proposed by Khayyer and Gotoh (2011) and Gotoh et al. (2014). The most important feature of this version of the model is the use of a higher-order error compensating term for the pressure Poisson equation (PPE). The model has been demonstrated to maintain the particle/pressure stability through the validation of several benchmarks. The 2D model was used by Wang et al.

(2016) for the seawall scours due to continuous actions of tsunami flows. Here we use 3D version of this model for the cylinder scour simulations. The following equations, although derived for the fluid phase, are also applicable to the sediment phase as well.

The governing equations include the mass and momentum conservation equations, closed by the Sub-Particle-Scale (SPS) turbulence model (Gotoh et al., 2001) to account for the turbulence scale smaller than the particle size, expressed as

$$\frac{1}{\rho} \frac{D\rho}{Dt} + \frac{\partial u_l}{\partial x_l} = 0 \quad (1)$$

$$\frac{Du_l}{Dt} = -\frac{1}{\rho} \frac{\partial p}{\partial x_l} + g_l + \nu_0 \frac{\partial^2 u_l}{\partial x_m \partial x_m} + \frac{1}{\rho} \frac{\partial \tau_{lm}}{\partial x_m} \quad (2)$$

where  $\frac{D}{Dt}$  denotes the full derivative;  $\rho$  is the density of fluid;  $u_l$  the spatially-filtered velocity;  $p$  the pressure;  $g_l$  the gravitational acceleration;  $\nu_0$  the kinematic viscosity;  $\tau_{lm}$  the SPS turbulent stress tensor, which can be calculated by the Boussinesq eddy viscosity assumption

$$\frac{\tau_{lm}}{\rho} = 2\nu_t S_{lm} - \frac{2}{3} k \delta_{lm} \quad (3)$$

where  $\nu_t$  denotes the turbulent eddy viscosity;  $S_{lm}$  the strain rate;  $k$  the SPS turbulent kinetic energy;  $\delta_{lm}$  the Kronecker's delta. According to Gotoh et al. (2001), the turbulent eddy viscosity can be evaluated by referring the Smagorinsky sub-grid scale model as

$$\nu_t = (C_s D)^2 |S| \quad (4)$$

$$|S| = (2S_{lm}S_{lm})^{1/2} \quad (5)$$

where  $C_s$  denotes the Smagorinsky constant around 0.1 ~ 0.24, and a value of 0.15 is used in this study;  $D$  the diameter of SPH particle, representing the resolved scale.

The two-step projection approach, i.e. prediction and correction, is used to solve the above governing equations. The flow field is updated by the time-marching procedure as

$$u_{lq}^{n+1} = u_{lq}^n + \Delta u_{lq}^* + \Delta u_{lq}^{**} \quad (6)$$

$$\Delta u_{lq}^* = \left( g_l + \nu_0 \frac{\partial^2 u_{lq}^n}{\partial x_m \partial x_m} + \frac{1}{\rho_q} \frac{\partial \tau_{lmq}^n}{\partial x_m} \right) \Delta t \quad (7)$$

$$\Delta u_{lq}^{**} = -\frac{1}{\rho_q} \frac{\partial P_q^{n+1}}{\partial x_l} \Delta t \quad (8)$$

where  $u_{lq}^n$  and  $u_{lq}^{n+1}$  denote the flow velocity at time level  $n$  and  $n + 1$ , respectively;  $q$  the phase indicator, indexed by C for the clear water and T for the sediment;  $\Delta u_{lq}^*$  the increment of velocity in the prediction step;  $\Delta u_{lq}^{**}$  the increment of velocity in the correction step. It should be noted that the upper case of pressure  $P$  in Eq. (8) already includes the trace of SPS stress tensor (Wang et al., 2016). According to Khayyer and Gotoh (2011) and Gotoh et al. (2014), a unified pressure Poisson equation can be used to represent the two-phase interactions. Here their most advanced CISP-HS-HL-ECS solution scheme of PPE is adopted, including the corrected ISPH with a higher-order Laplacian, and a higher-order and error-compensating source term to minimize the instantaneous and accumulative projection-based errors.

Following SPH summation principle, the density of particle at time level  $n$  is calculated by the integral interpolation theory as

$$\rho_i^n = \sum_j^N M_j W(|\mathbf{r}_j^n - \mathbf{r}_i^n|, h) = \sum_j^N M_j W_{ij}^n \quad (9)$$

where  $i$  and  $j$  denote the objective particle and its neighbors, respectively;  $M$  the mass of particle;  $N$  the number of neighboring particles;  $\mathbf{r}$  the coordinate vector of particle;  $h$  the smoothing length, which is taken as 1.2 times of the particle diameter;  $W$  the kernel function, where a cubic B-spline function is used (Monaghan, 1992).

The discretization of pressure gradient, SPS turbulent stress and kinematic viscosity terms of Eq. (2) follows the standard SPH rules (Shao and Lo, 2003; Gotoh et al. 2004) as

$$\left. \frac{\nabla P}{\rho} \right|_i = \sum_{j \neq i}^N M_j \left( \frac{P_j}{\rho_j^2} + \frac{P_i}{\rho_i^2} \right) \left. \frac{\partial W_{ij}}{\partial x_l} \right|_i \quad (10)$$

$$\left. \frac{1}{\rho} \frac{\partial \tau_{lm}}{\partial x_m} \right|_i = \sum_{j \neq i}^N M_j \left( \frac{\tau_{lmj}}{\rho_j^2} + \frac{\tau_{lmi}}{\rho_i^2} \right) \left. \frac{\partial W_{ij}}{\partial x_m} \right|_i \quad (11)$$

$$v_0 \left. \frac{\partial^2 u_l}{\partial x_m \partial x_m} \right|_i = v_0 \sum_{j \neq i}^N M_j \left( \frac{8\rho_j}{(\rho_i + \rho_j)^2} S_{lm} \right) \left. \frac{\partial W_{ij}}{\partial x_m} \right|_i \quad (12)$$

By adopting a hybrid scheme combining the SPH first derivative and finite difference formulation, the Laplacian of PPE in Eq. (9) is represented as

$$\left. \frac{\partial}{\partial x_l} \left( \frac{1}{\rho} \frac{\partial P}{\partial x_l} \right) \right|_i = \sum_{j \neq i}^N M_j \frac{8}{(\rho_i + \rho_j)^2} \frac{P_{ij} r_{lij}}{r_{mij} r_{mij}} \left. \frac{\partial W_{ij}}{\partial x_l} \right|_i \quad (13)$$

where  $P_{ij} = P_j - P_i$  and  $r_{lij} = r_{lj} - r_{li}$  are defined, respectively.

## 2.2 3D ISPH sediments solver

Prior to deriving the 3D sediment erosion model, it would be useful to have a brief review on the 2D ISPH erosion model using the Turbidity Water Particle (TWP) scheme (Wang et al., 2016). The fundamental idea of TWP is that the whole simulation media is divided into different types of particles, which are defined as: dummy particles to compensate the kernel deficiency near solid boundary; clear water particles to represent the water flow; inlet and outlet particles to close the upstream and downstream boundaries; interface wall particles to sustain the pressure of inner water particles and provide candidates of the eroded particle; and mostly important, Turbidity Water Particles (TWPs) represent the mixture of water-sediment particles after they are eroded from the movable bed.

The TWPs obtain their initial densities once they are eroded off, i.e. at the moment when they are transformed from the interface wall particles to the TWPs. Since these are the mixtures of water and sediment, their initial density should fall somewhere between the clear water and sediment grain. In some documented SPH sediment studies, such as by Hayashi et al. (2003), a fixed value of  $2650 \text{ kg/m}^3$  was used for the sediment particles. In reality the sediment particles are always mixed with the clear water. Also the computational SPH particle size is always much larger than the sediment grain diameter. Therefore, it is not appropriate to assume the SPH sediment particle density to be equal to the sediment grain density, i.e.  $2650 \text{ kg/m}^3$ . By assuming a saturated sediment layer and a sand porosity of about 0.53, the bulk density of the granular phase adopted for the SPH computations in Manenti et al. (2012) was equal to  $1750 \text{ kg/m}^3$ . However, accurate evaluation of the initial density of TWPs is not straightforward, although Sumer et al. (1996) and Soulsby and Damgaard (2005)

provided some theoretical analysis.

In the present 3D ISPH sediment erosion model, the initiation of sediment grain follows the counterbalance between the critical sediment resistance and flow shear stress acting on the IWPs. Every sediment particle at the bottom is initially fixed (i.e. excluded from the SPH computations) and may be eroded, regardless of its initial status, if the failure criterion is satisfied depending upon the flow evolutions, by following Manenti et al. (2012). In principle, the flow shear stress should be calculated from the turbulent stress term in Eq. (2), if the sufficiently refined SPH particle size were to be used. However, this is usually not achievable in the practice. Relatively coarse SPH particles combined with the SPS turbulent model could not accurately predict the flow turbulent quantities, according to the latest study of Kazemi et al. (2017) for open channel flows over a rough bed. Therefore, we will use the gradient of resolved velocity field to compute the flow shear stress near the sediment bed, by following Manenti et al. (2012), but shift the center of zero-velocity datum to the dummy particle layer rather than on the interface wall particle layer. This procedure is used to avoid the numerical errors, as implemented for the 2D simulations in Wang et al (2016).

Accurate determination of critical shear stress in a complex 3D domain is crucial to the sediment inception. Here the benchmark Shields' formula is used but additional corrections are made to improve its performance on longitudinal and transverse slopes. To do this, the sediment inception theory of Dey (2003) is modified and adopted in the SPH sediment erosion model. A local coordinate system for each individual SPH particle is established and x-axis of the local and global coordinates is defined within the same gravitational plane. By use of this, it could effectively avoid the randomness of directional angle in Dey's (2003) original formulation, and therefore guarantee the same set of solution procedures on the SPH particles in the computation. This leads to unified equation forms and straightforward numerical programs. It should be noted that the main contribution here is the establishment of the local and global coordinate systems to include the benchmark theory of Dey (2003) into the proposed 3D ISPH framework, therefore developed an accurate sediment erosion model with the evaluation of key calculation parameters as shown in the Appendix. The fundamental sediment theories of Dey (2003), however, were kept unchanged.

A schematic diagram of the sediment inception model is shown in Fig. 1, in which the global horizontal plane  $S$  is assigned to denote the horizontal coordinate plane  $x$ - $y$  and the local plane  $S'$  denotes the tangential plane of the scour hole edge at the position of an interface particle  $P$ . For each interface bed particle  $P$ , a moving-least-square (MLS) approach is adopted to find the normal vector of the local plane  $S'$  from the coordinates of its neighboring IWPs located inside its SPH support of particle  $P$ . A local coordinate  $x'$  is then defined from the intercept of plane  $S'$  and a vertical plane that is parallel with the vertical coordinate plane  $x$ - $z$  and passing through the point  $P$ . It is apparent that the projection of the local coordinate  $x'$ -axis onto the global coordinate plane  $S$  is parallel to its global  $x$ -axis. Based on this definition,  $\alpha$  and  $\beta$  are defined as the angles between  $S'$  and  $S$  in the  $y$ - $z$  and  $x$ - $z$  planes, respectively.  $\gamma$  is defined as the angle on the  $S'$  plane between the horizontal

tangential component of the flow velocity and the local coordinate of  $x'$ -axis, with the positive downwards directed. The detailed calculation procedures of these angles are provided in Appendix.

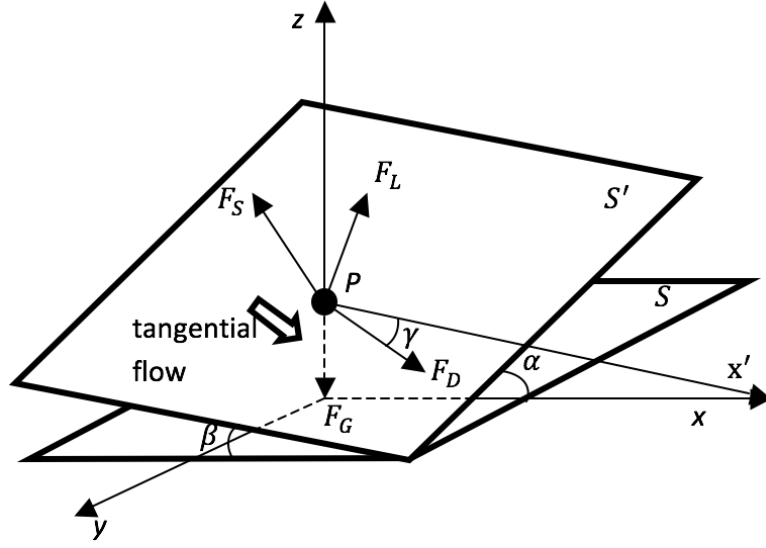


Fig. 1 Schematic diagram of sediment inception and layout of local and global coordinates

By force analysis at particle P in Fig. 1,  $F_G$  is the gravitational force,  $F_D$  the fluid drag force along the slope,  $F_L$  the lifting force and  $F_S$  the static Coulomb frictional force between particle P and the sloping bed. When particle P reaches the threshold condition of motion, the force balance requires

$$F_S^2 = (F_G \sin \beta + F_D \cos \gamma)^2 + (F_G \sin \alpha + F_D \sin \gamma)^2 \quad (14)$$

The critical Coulomb frictional force at the sediment initiation is

$$F_S = (F_G \sqrt{\cos^2 \beta - \sin^2 \alpha} - F_L) \mu_c \quad (15)$$

where  $\mu_c$  is the static Coulomb frictional coefficient, related to the sediment underwater repose angle  $\phi$ . By solving Eqs. (14) and (15) we have

$$F_D^2 + 2F_D F_G (\cos \gamma \sin \beta + \sin \gamma \sin \alpha) + F_G^2 (\sin^2 \beta + \sin^2 \alpha) - (F_G \sqrt{\cos^2 \beta - \sin^2 \alpha} - F_L)^2 \tan^2 \phi = 0 \quad (16)$$

which can be further represented by

$$(1 - \eta^2 \tan^2 \phi) \hat{\tau}_{cs}^2 + \frac{2}{\hat{F}_D} (\cos \gamma \sin \beta + \sin \gamma \sin \alpha + \eta \tan^2 \phi \sqrt{\cos^2 \beta - \sin^2 \alpha}) \hat{\tau}_{cs} - \frac{1}{\hat{F}_D} [(\cos^2 \beta - \sin^2 \alpha) \tan^2 \phi - \sin^2 \beta - \sin^2 \alpha] = 0 \quad (17)$$

$$\hat{F}_D = \frac{6F_D}{(\pi \rho d^2 u_{*cs}^2)} \quad (18)$$

$$\eta = F_L / F_D \quad (19)$$

where  $\hat{\tau}_{cs}$  is the non-dimensional critical shear stress of sediment on a slope, which can also be written as  $\rho u_{*cs}^2 / [d(\rho_P - \rho)g]$  or  $\tau_{cs} / [d(\rho_P - \rho)g]$  ( $\rho_P$  is the density of particle P). Here  $u_{*cs}$  is the critical frictional velocity ( $\sqrt{\tau_{cs} / \rho}$ ) in the tangential direction on a slope and  $\tau_{cs}$  is

the corresponding critical shear stress. Dey (2003) assumed a value of 0.85 for the force ratio  $\eta$  (which is also followed here) and obtained the explicit solution as

$$\hat{\tau}_{cs} = \frac{1}{(1-\eta^2 \tan^2 \phi) \hat{F}_D} \left\{ -(\cos \gamma \sin \beta + \sin \gamma \sin \alpha + \eta \tan^2 \phi \sqrt{\cos^2 \beta - \sin^2 \alpha}) + \left[ (\cos \gamma \sin \beta + \sin \gamma \sin \alpha + \eta \tan^2 \phi \sqrt{\cos^2 \beta - \sin^2 \alpha})^2 + (1 - \eta^2 \tan^2 \phi)(\cos^2 \beta \tan^2 \phi - \sin^2 \alpha \tan^2 \phi - \sin^2 \beta - \sin^2 \alpha) \right]^{0.5} \right\} \quad (20)$$

Further normalizing Eq. (20) with regard to the critical shear stress for a horizontal bed  $\hat{\tau}_{co}$  leads to

$$\hat{\tau}_c = \frac{1}{(1-\eta \tan \phi) \tan \phi} \left\{ -(\cos \gamma \sin \beta + \sin \gamma \sin \alpha + \eta \tan^2 \phi \sqrt{\cos^2 \beta - \sin^2 \alpha}) + \left[ (\cos \gamma \sin \beta + \sin \gamma \sin \alpha + \eta \tan^2 \phi \sqrt{\cos^2 \beta - \sin^2 \alpha})^2 + (1 - \eta^2 \tan^2 \phi)(\cos^2 \beta \tan^2 \phi - \sin^2 \alpha \tan^2 \phi - \sin^2 \beta - \sin^2 \alpha) \right]^{0.5} \right\} \quad (21)$$

where  $\hat{\tau}_c$  is defined as the ratio of critical shear stress on a slope to that on a horizontal plane.

For unidirectional open channel flow, the direction of flow on sloping bed is tangentially downwards, and further simplification can be made on Eq. (21) by using  $\gamma = 0$ , leading to

$$\hat{\tau}_c = \frac{1}{(1 - \eta \tan \phi) \tan \phi} \left\{ -(\sin \beta + \eta \tan^2 \phi \sqrt{\cos^2 \beta - \sin^2 \alpha}) + \left[ (\sin \beta + \eta \tan^2 \phi \sqrt{\cos^2 \beta - \sin^2 \alpha})^2 + (1 - \eta^2 \tan^2 \phi)(\cos^2 \beta \tan^2 \phi - \sin^2 \alpha \tan^2 \phi - \sin^2 \beta - \sin^2 \alpha) \right]^{0.5} \right\} \quad (22)$$

In summary, during the 3D ISPH sediment computations, if the ratio of fluid shear stress computed at particle P over the sediment threshold shear stress for a horizontal bed as computed by the Shields' curve is larger than the critical value as specified by Eq. (22), i.e. if  $\tau_{bP}/\tau_c \geq \hat{\tau}_c$ , then the interface bed particle P is regarded to be erodible and changed into TWP. TWPs are moved by the N-S equations and their densities are updated at each time step following Eq. (9) while mixing with the other clear water or TWP particles. The fluid shear stress  $\tau_{bP}$  is calculated by the following formula, as proposed by Wang et al. (2016)

$$\frac{\tau_{bP}}{\rho} = (\kappa D)^2 \left( \frac{u_{bP}}{D} \right)^2 \quad (23)$$

where  $\kappa$  is the von Karmon constant (0.4);  $D$  the SPH particle size; and  $u_{bP}$  the tangential velocity component of the flow.

### 2.3 Treatment of free surfaces and solid boundaries

The treatment of free surfaces simply follows that presented by Shao and Lo (2003). Here a brief summary is provided. If the density of a particle is 10% below its reference

density, it can be judged as the surface particle. Then a zero pressure is imposed as the boundary condition. The majority of the free surface particles can be easily and correctly identified. Although some misjudgments can be made, this has no substantial influence on the global accuracy.

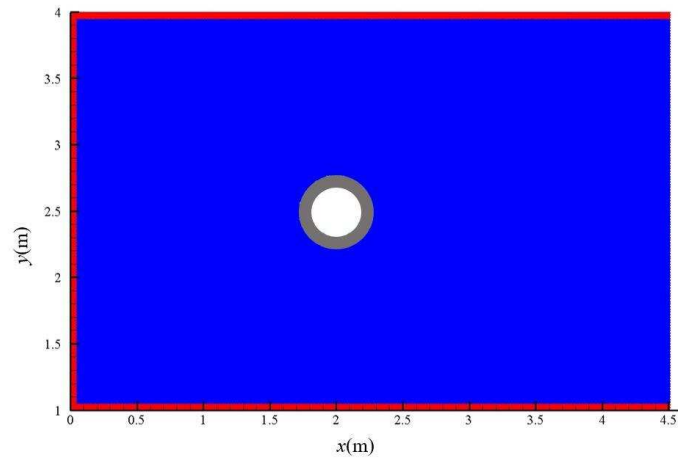
The impermeable and fixed walls are modeled by the particles which are fixed along the solid boundaries. In ISPH computations, the PPE is solved on these wall particles with the imposition of zero pressure gradient between the dummy and wall particles, thereby satisfying the Neumann boundary condition. If the dummy particle positions are fixed, an equivalent of non-slip boundary is enforced. The density of dummy particle, i.e. DMP, is always kept at  $1000 \text{ kg/m}^3$ , while its pressure is set to the pressure value of neighboring wall particles in the normal direction during the pressure solution. So the pressure of DMPs should vary in the computations.

### **3. ISPH Fluids Model Validation - Flow Passing a Cylinder over Fixed Bed**

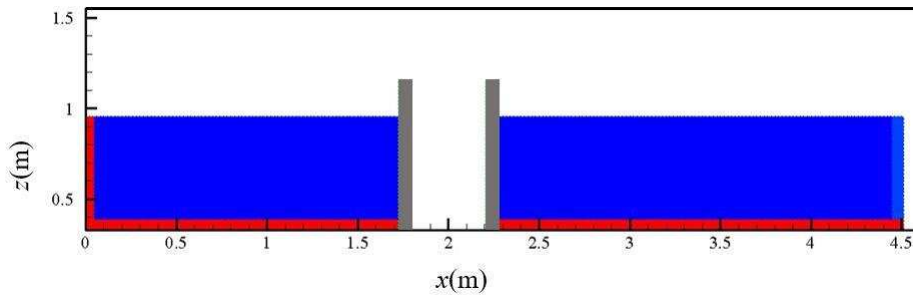
Before applying the ISPH erosion model for the local scour around a vertical cylinder, we first validate the 3D fluids model by using the fixed-bed experiment of Roulund et al. (2005), for a steady current passing around a vertical cylinder. According to Roulund et al. (2005), the flows demonstrated the following three features: (1) formation of the horseshoe vortices in front of the cylinder; (2) formation of the vortex flows in form of vortex shedding on the lee-side of the cylinder; (3) contraction of the flow streamlines on lateral side of the cylinder. These hydrodynamic processes, combined with the down-flows in front of the cylinder, are the dominant factors to account for the sediment transport and associated local scouring. Therefore, accurate modelling of the flow field can provide useful information on the sediment erosion process.

#### **3.1 Model setup and computational parameters**

The present 3D ISPH water flow simulation is based on Roulund et al. (2005), in which the fixed-bed experiment was carried out for a steady current flow. The experimental flume was 35 m long, 3 m wide and the diameter of the cylinder was 53.6 cm. A smoothed bed condition was considered. The uniform flow depth was maintained at 54 cm and the averaged inflow velocity was 32.6 cm/s. In the ISPH model setup, most computational parameters followed the physical ones, except that the length of the flume was reduced to 4.5 m (about 8 times of the cylinder diameter) to save CPU expense. As a result, the cylinder was located 2.0 m from the numerical flow inlet. A sensitivity analysis has found that as long as the length of the flume is more than 8 times of the cylinder diameter, almost identical flow patterns can be obtained. The schematic setup of the numerical domain is shown in Fig. 2 (a) and (b), respectively, for the plan and side views. The origin of the vertical coordinate starts at the bed surface of  $z = 0.4 \text{ m}$ .



(a) Plan view



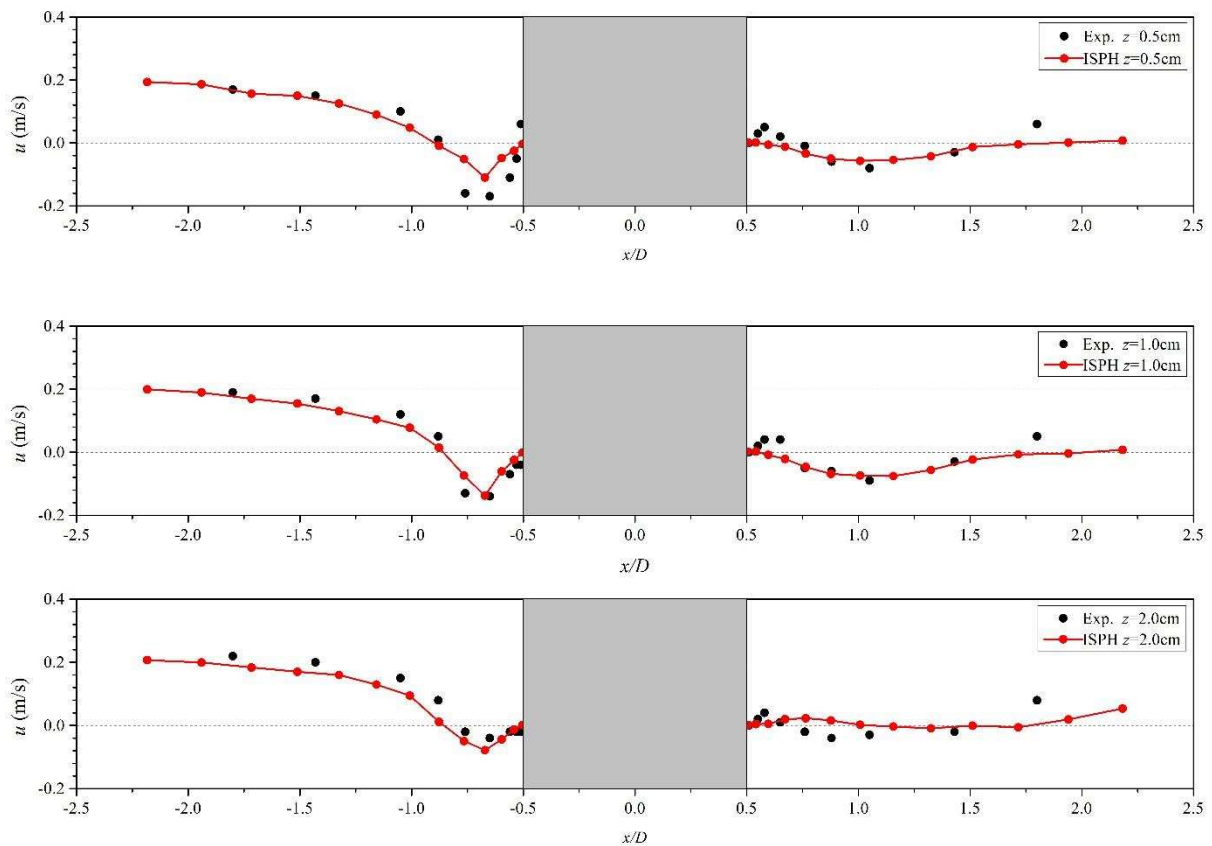
(b) Side view

Fig. 2 Schematic setup of numerical domain for flow passing a cylinder over fixed bed, including non-erodible bed particles (in red), non-erodible cylinder wall particles (in grey) and inner water particles (in blue)

The ISPH particle spacing is 0.02 m considering both the computational efficiency and accuracy. The inflow/outflow boundary conditions are treated by using the concept of soluble particle wall, as proposed by Wang et al. (2016). To ensure the flow to be fully developed after entering the computational domain, a logarithmic velocity profile as calibrated by the experimental data of Roulund et al. (2005) is imposed at the inflow boundary. The outflow boundary is treated as the normal open boundary, where the SPH particles keep their properties and move out freely with zero gradient of the horizontal velocity. A series of numerical gauges are placed in the centreline of the flume along the flow direction, which are used to extract both the longitudinal and vertical velocities for the time series. The velocity gauges are placed at 25 locations along the flow direction, at  $z = 0.5, 1.0, 2.0, 5.0, 10.0$  and  $20.0$  cm, respectively, covering the front and rear sides of the cylinder in Roulund et al.'s experiment. Here to be consistent with Roulund et al. (2005),  $z$  has been redefined relative to the bed surface.

### 3.2 Model validations on velocity and pressure

Figs. 3 and 4 show the measured (Roulund et al. 2005) and ISPH computed horizontal and vertical velocities at different vertical locations of  $z$  along the centerline of flume in the flow direction. It is shown from Fig. 3 that on the upstream side of the cylinder, there is a general good agreement between the numerical simulations and experimental measurements, although the  $u$ -velocities at smaller and larger values of  $z$  very near to the cylinder are somewhat under-predicted. The same phenomenon was also observed in the 3D high-resolution Eulerian grid modeling of Roulund et al. (2005). It is promising to note that ISPH computations also well captured the flow velocities after the cylinder at very small  $z$  locations, which has been difficult to reproduce by the numerical models. On the other hand, Fig. 4 shows that the 3D ISPH computations could accurately reproduce the downward flow velocities in front of the cylinder. Also some smaller scale downflows are also captured on the rear side of the structure. However, due to the influence of the shedding vortices, the simulated downflows are not stable. Compared with the high-accuracy grid simulations made by Roulund et al. (2005), in which a more refined vertical spacing of 0.008 m was used, the ISPH model used a particle size of 0.02 m and achieved equally good performance. This could be attributed to the robustness of mesh-free numerical scheme of ISPH in simulating the complex 3D flow structures.



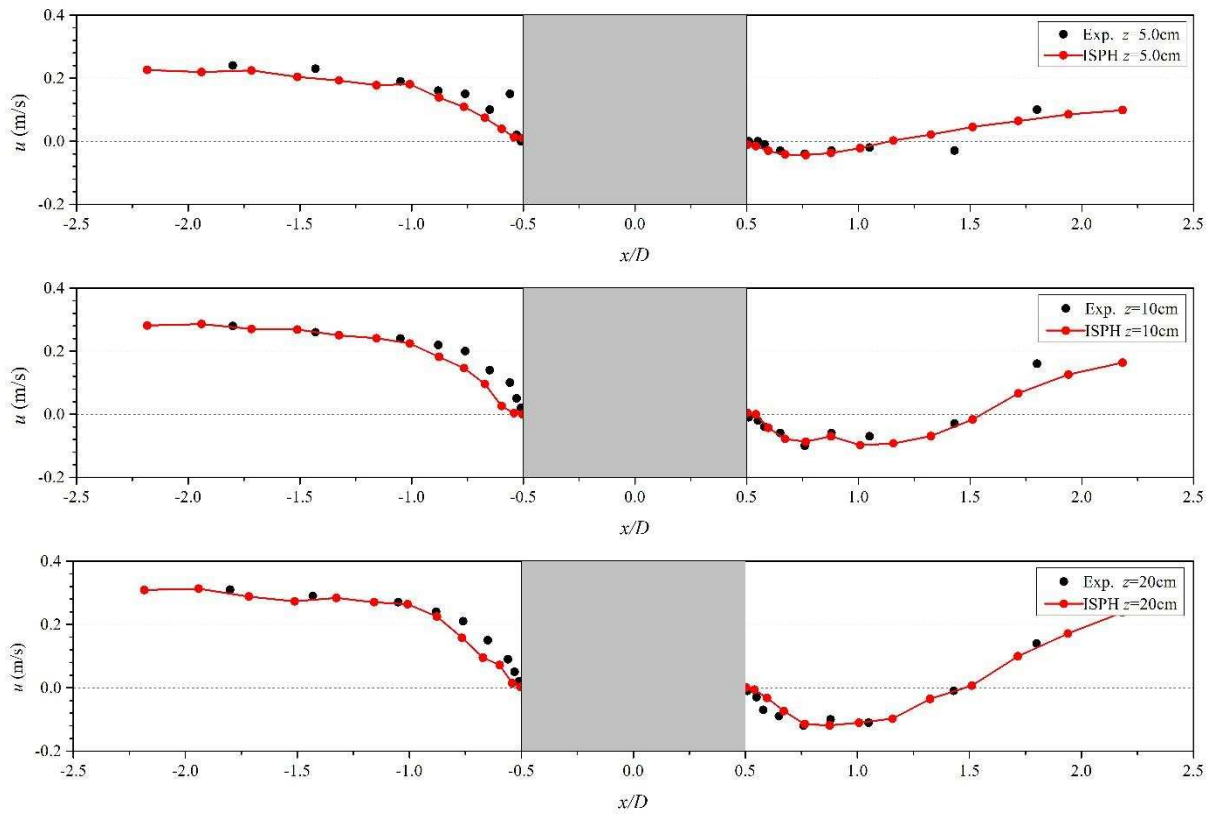
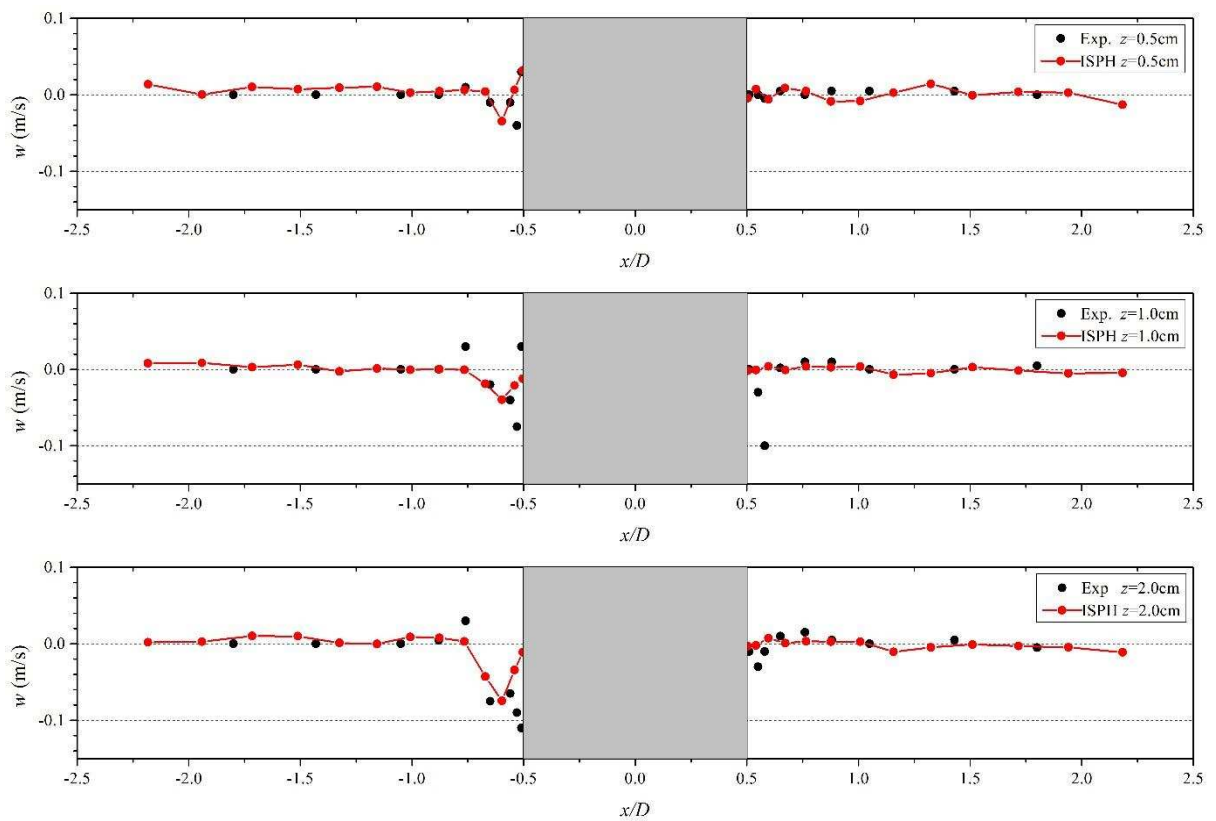


Fig. 3 Measured and ISPH horizontal velocities  $u$  at different vertical locations  $z$



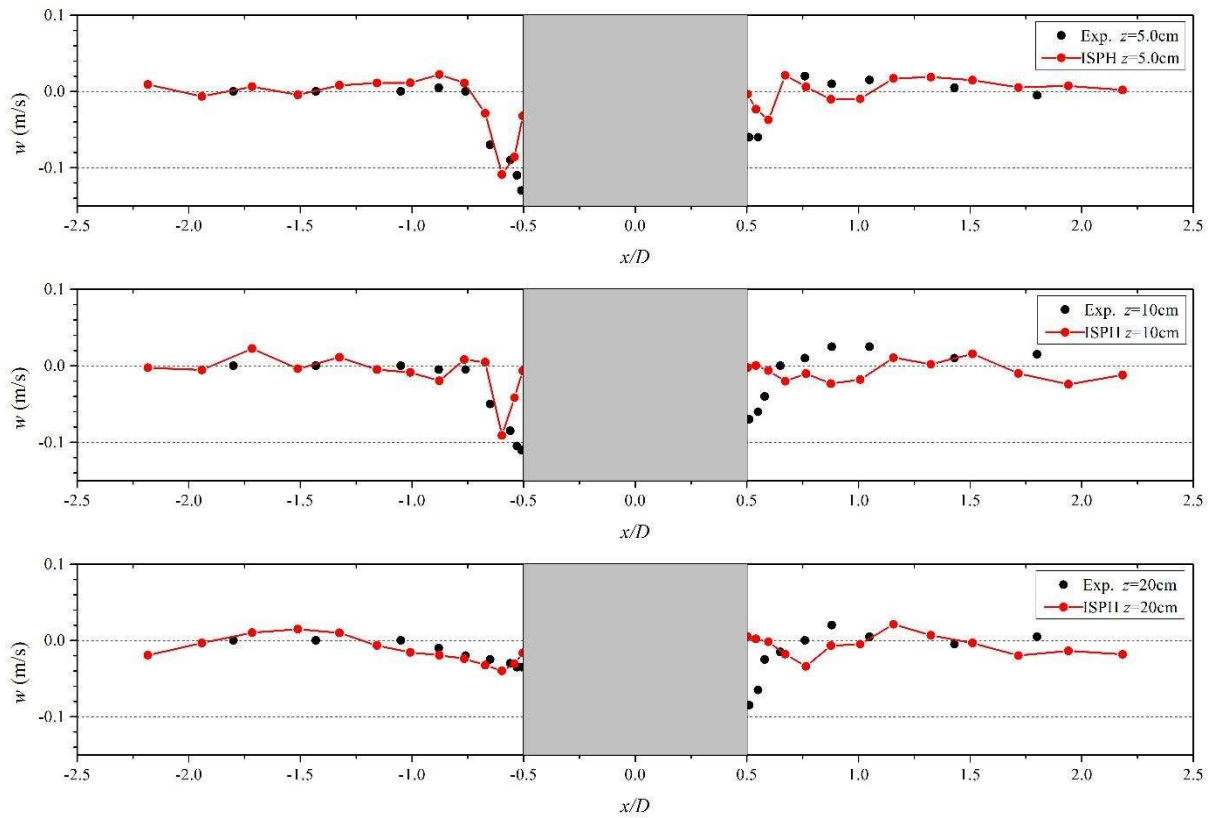
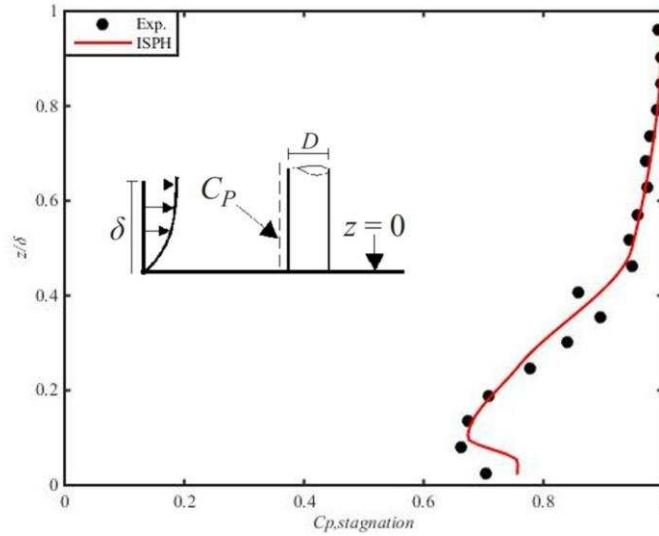
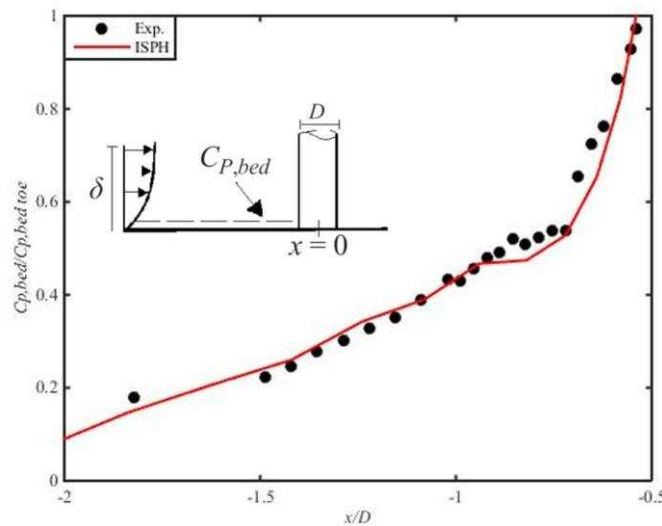


Fig. 4 Measured and ISPH vertical velocities  $w$  at different vertical locations  $z$

For a quantitative evidence of the robust pressure solution schemes of CISP-HS-HL-ECS as proposed by Khayyer and Gotoh (2011) and Gotoh et al. (2014) in the application of flow passing around a vertical cylinder, Fig. 5 (a) and (b) compares the present ISPH simulation results with the documented data of Roulund et al. (2005), in which Fig. 5 (a) presents the stagnation pressure across the flow depth on the upstream side of the cylinder and Fig. 5 (b) presents the pressure on the bed along the upstream centreline. In both cases, the normalized pressure coefficient,  $C_P$ , is used to interpret the numerical results by following the definitions of Roulund et al. (2005). Once again the agreement is quite satisfactory and the accuracy of the model is further demonstrated.



(a) Stagnation pressure across the flow depth, following Roulund et al. (2005)



(b) Pressure on bed along the upstream centreline, following Roulund et al. (2005)

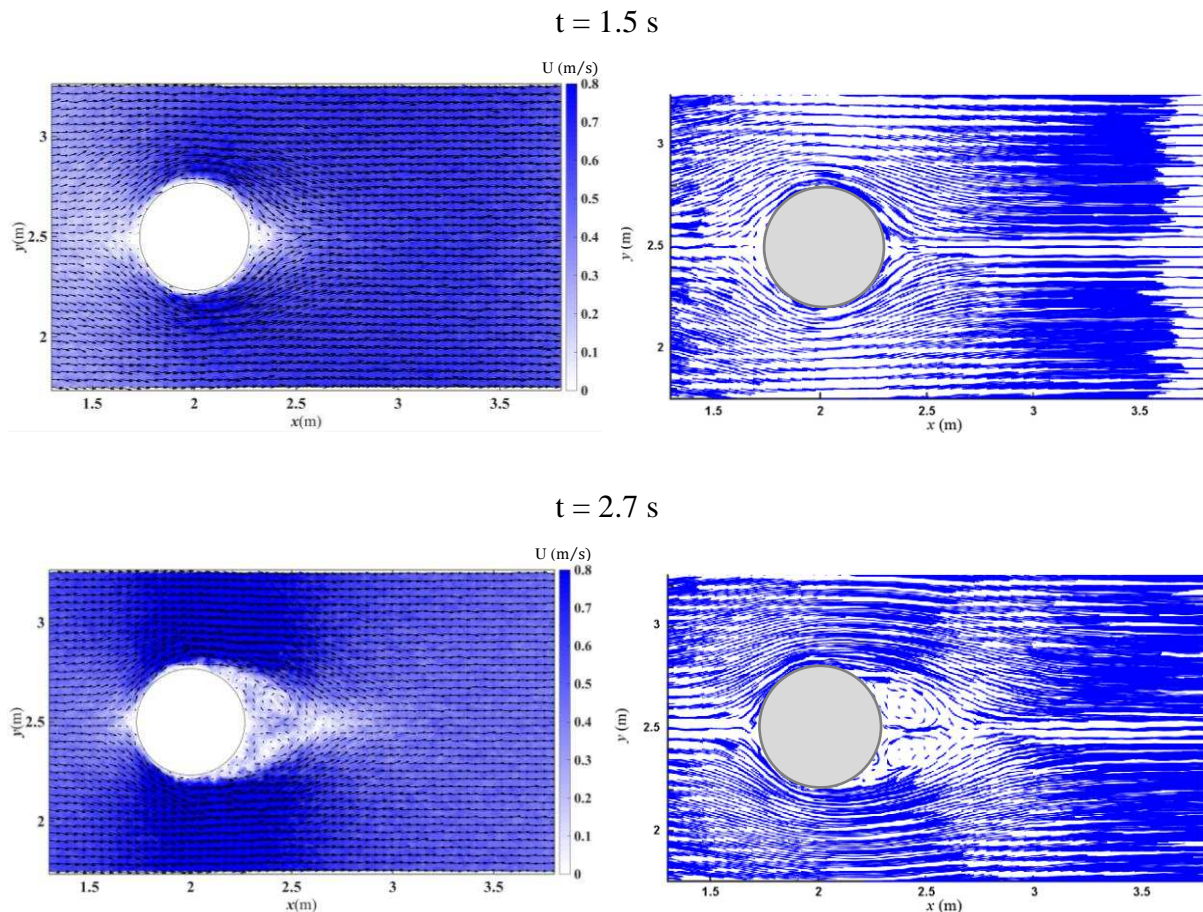
Fig. 5 Comparisons of pressure coefficient between ISPH results and documented data of Roulund et al. (2005)

### 3.3 Results and discussions on vortices

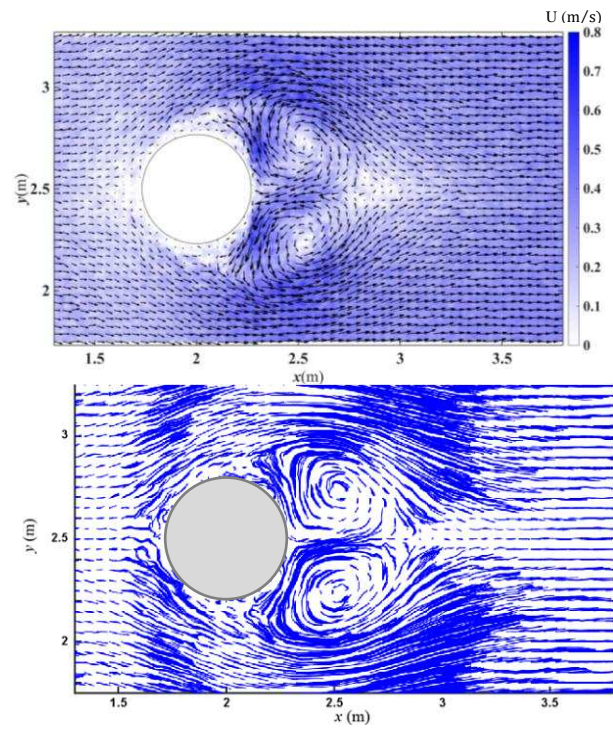
According to Roulund et al. (2005), the lee-wake vortices are generated by changes in the boundary layer on the cylinder surface. The shear layers emanating from the side edges of cylinder could roll up to form the lee-wake vortices. Fig. 6 (a) and (b) show the time sequences of velocity vector and streamline of the lee-wake vortices at vertical location  $z = 0.24 \sim 0.26$  m which is near the middle of flow depth, when the flow passing around the cylinder. It clearly indicates the formation of lee-wake vortices which further transform into two large circulation zones. This vortex zone is convected with the flows into the downstream direction and its dimension is gradually dampened out due to the viscosity of water. Then a

new pair of the vortex area appears again in the next flow cycle. Generally speaking, the evolution of lee-wake vortices demonstrates somewhat unsteady behaviors.

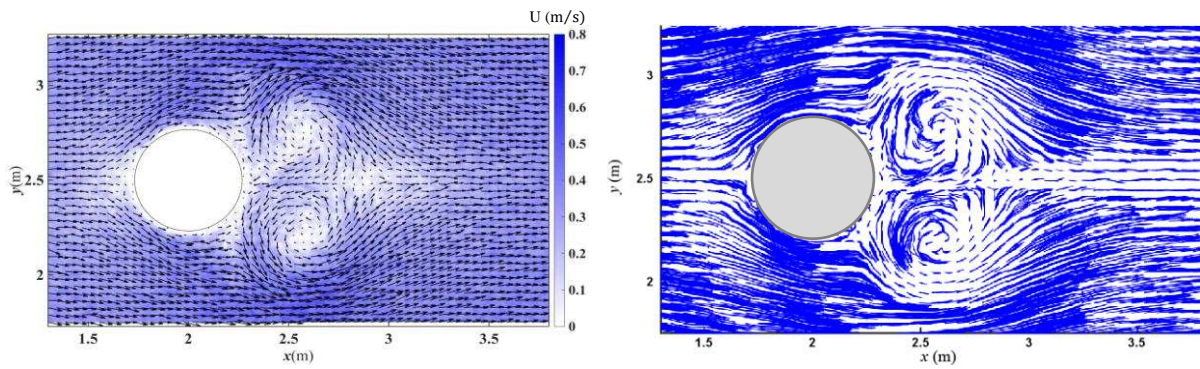
It should be noted that the present Re number is around 174736, at which the lee-wake vortices should demonstrate somewhat asymmetric behaviors, according to Roulund et al. (2005). This is not clearly reproduced in the ISPH simulations. The main reason could be attributed to the relatively coarse SPH particle resolution, which prevented the correct reproduction of the physical turbulence fluctuation and resulted in a more symmetric vorticity field. On the other hand, although the adopted sub-particle-scale (SPS) turbulence model (Gotoh et al., 2001) represents a benchmark in the SPH turbulence, further improvement is still required since it also significantly influenced the generation of asymmetric vortices. Even though, the SPS turbulence model has already demonstrated its promising performance in capturing most of the large scale vortices and wake fields as shown in Fig. 5. Especially, some minute evidences of the asymmetric vortices could be sensed at time  $t = 2.7$  s during the early stage of the flow process (on the right column).



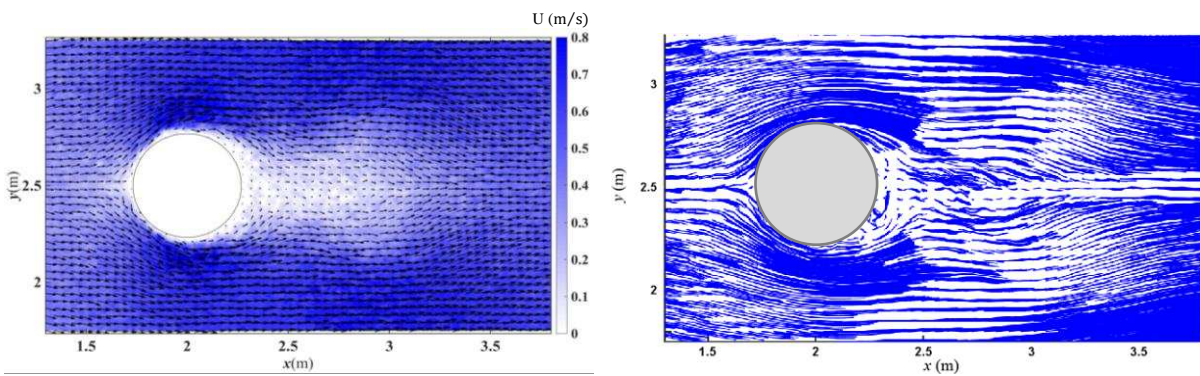
$t = 4.0 \text{ s}$



$t = 5.3 \text{ s}$



$t = 6.5 \text{ s}$



$t = 7.5 \text{ s}$

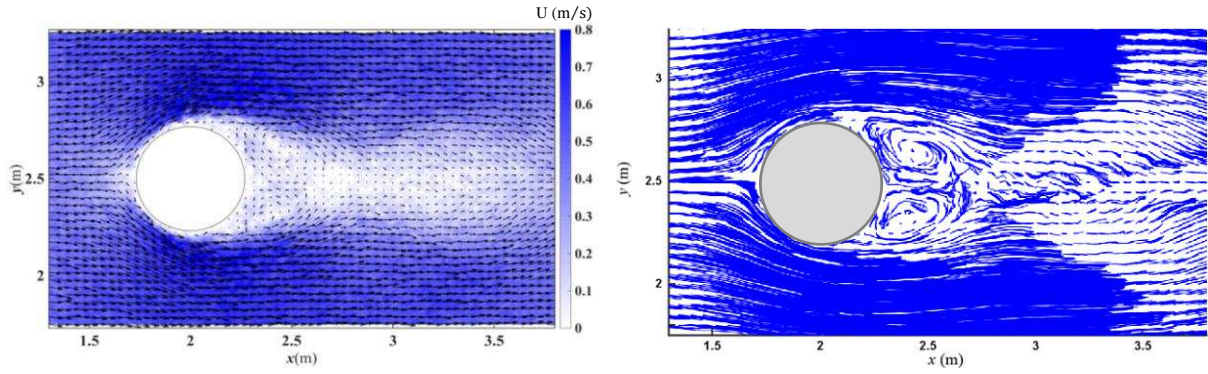
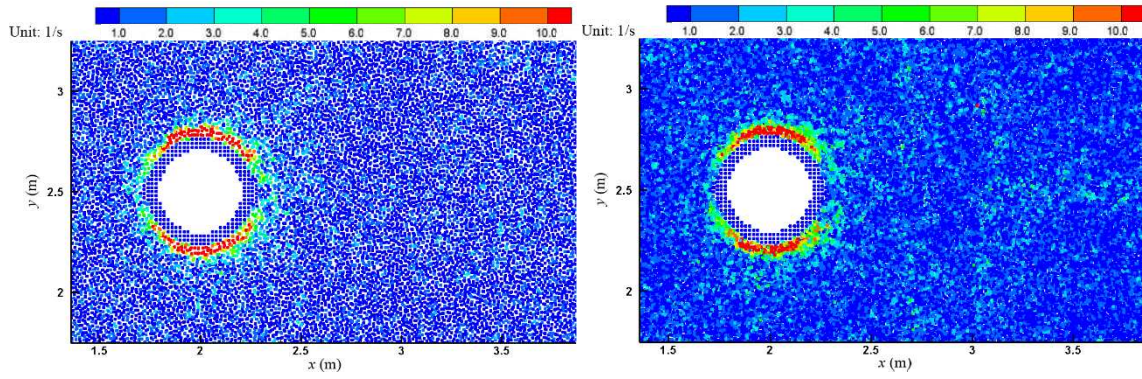


Fig. 6 Time sequences of (a) velocity vector (left column); and (b) streamline (right column) of lee-wake vortices near middle flow depth at  $z = 0.24 \sim 0.26$  m

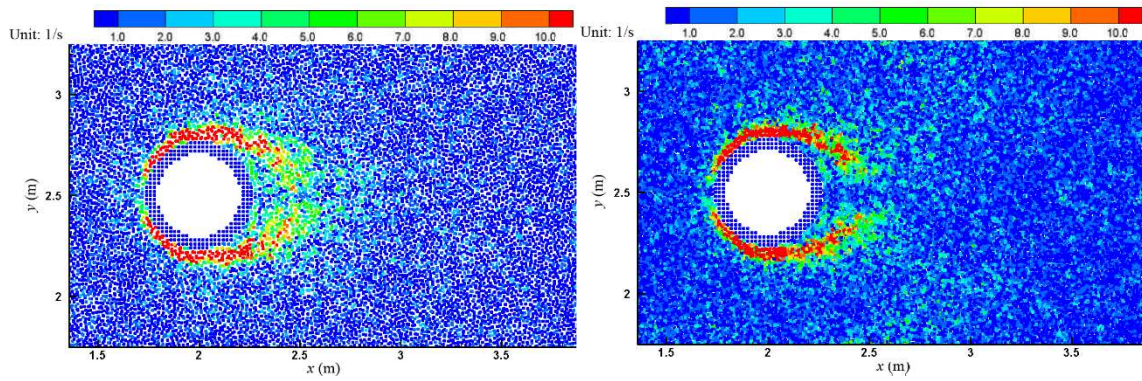
Due to the non-uniformity of velocity distributions along the flow depth near the cylinder, the evolutions of lee-wake vortices also change vertically, and the dimension of vortices increases towards the water surface. Fig. 7 shows the plan view of lee-wake vortices near middle flow depth ( $z = 0.24 \sim 0.26$  m) and channel bed ( $z = 0.0 \sim 0.02$  m) in time series. It shows the periodic evolution of the vortices that form initially on the lateral sides of the cylinder and then extend gradually to the front and rear sides. The shedding vortices on the rear of cylinder develop and spread out further downstream in the form of smaller eddies. Following the dissipation of these eddies through the flow viscosity, new vortices appear again on the lateral sides of the cylinder. Comparing with the two columns of sub-figures, it is shown that the scale of near-bed vortices is for most time smaller than that of the near-surface ones. Besides, the last two sub-figures at time  $t = 7.5$  s even disclosed the presence of horseshoe vortices, and their shapes and locations have been distinctly identified by the 3D ISPH computations. However, some kinds of data noise could be seen in Fig. 7 due to the following two reasons, i.e. the instantaneous value of the vortices field and the lack of sufficient SPH particles existing on the reference plane that is used for the plotting.

On the other hand, the horseshoe vortices in front of the cylinder are generated by the incoming flow, during which the boundary layer on the bed upstream of the cylinder experiences the separation. The separated boundary layer rolls up to form horseshoe vortices around the cylinder, and trails off in the downstream direction. Previous studies found that the development of horseshoe vortices increased with the intensity of flow turbulence, i.e. Reynolds number. Fig. 8 shows the ISPH computed near-bed velocity field around the cylinder and the formation of down flows on the front. However, the flow velocity is greatly reduced on the rear side due to the sheltering effect of the structure. The flows even demonstrate the upstream velocity from the influence of lee-wake vortices. In general, the proposed 3D ISPH water model has satisfactorily reproduced the vortex structures and their evolutions around the cylinder on fixed channel bed.

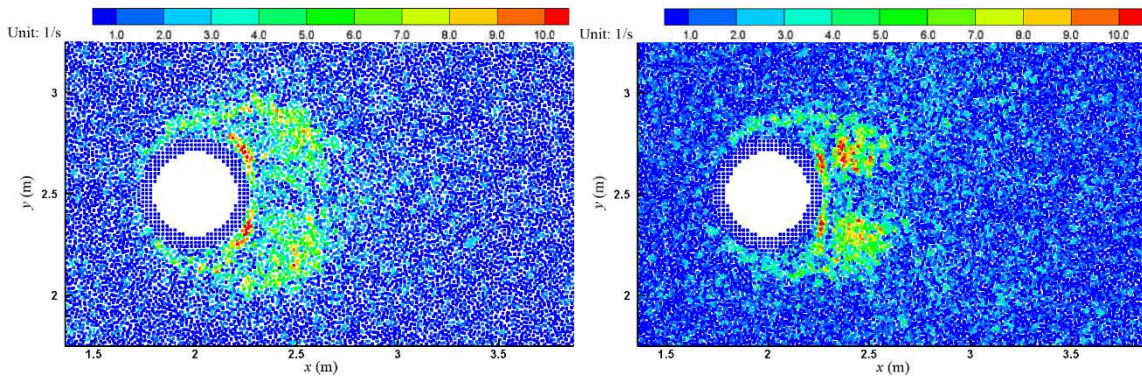
$$t = 1.5 \text{ s}$$



$t = 2.7 \text{ s}$



$t = 4.0 \text{ s}$



$t = 5.3 \text{ s}$

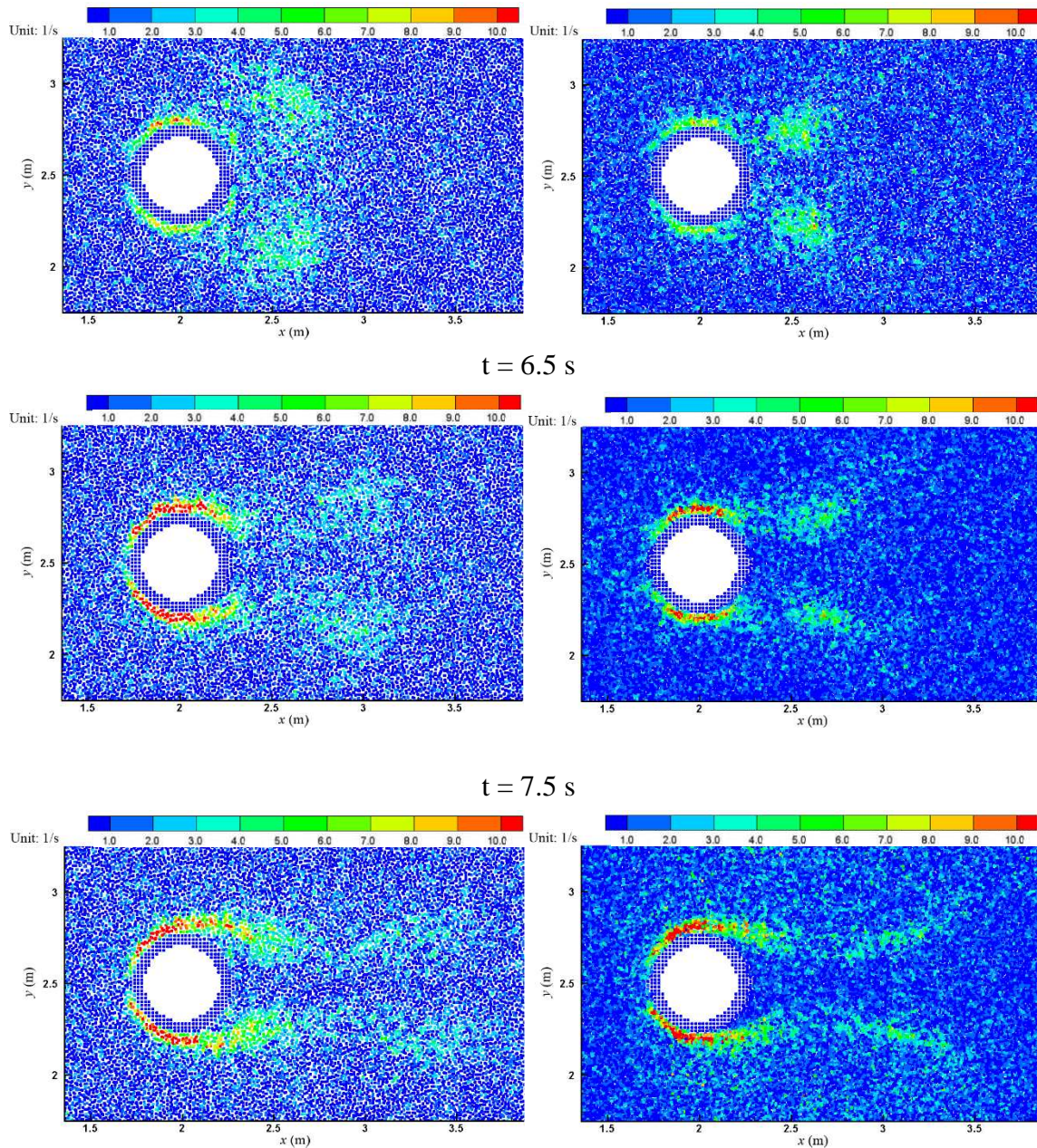


Fig. 7 Time sequences of lee-wake vortices (a) near middle flow depth at  $z = 0.24 \sim 0.26$  m (left column); and (b) near channel bed at  $z = 0.0 \sim 0.02$  m (right column)

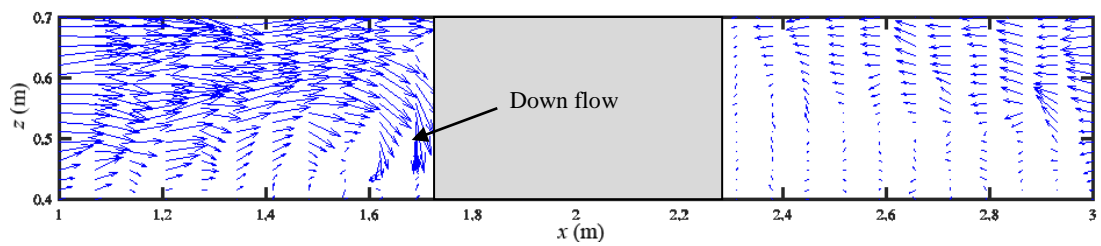


Fig. 8 ISPH computed near-bed velocity field around cylinder

### 3.4 3D representation of pressure field

Finally, the computed 3D pressure field at the stable stage of the flow is shown in Fig. 9, for the illustration purpose. It shows that the pressure patterns are quite stable and free of noises, and distributed in a trend consistent with the quantitative pressure validations as shown in Fig. 5. That is to say, due to the existence of horseshoe vortices, the vertical pressure coefficient increases from the bottom to the surface, and the horizontal one increases along the flow direction from the inlet to the cylinder location. This further evidenced the robust pressure solution scheme of CISPH-HS-HL-ECS (Khayyer and Gotoh, 2011; Gotoh et al., 2014).

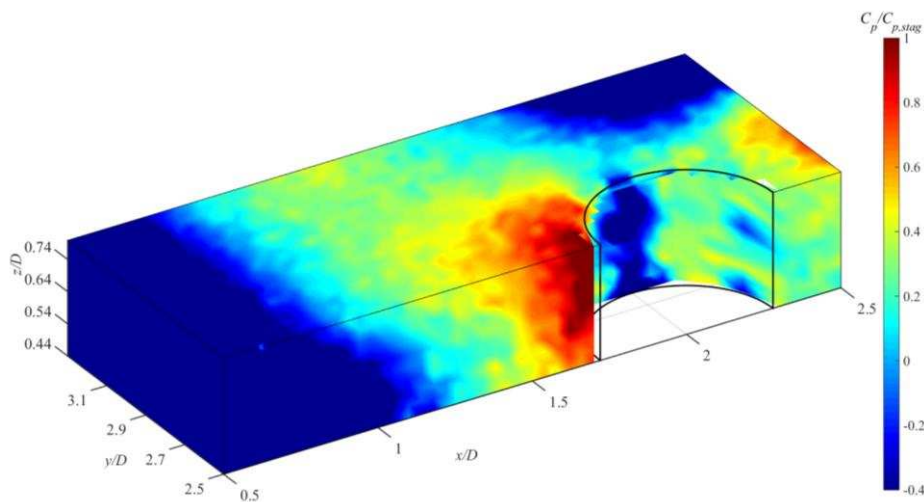


Fig. 9 3D representation of the pressure field

## 4. Laboratory Experiment on Local Scour around a Vertical Cylinder

An experiment on the local sediment bed scour around cylinder was carried out in a laboratory flume under the unidirectional flow condition at Port and Coastal Engineering Laboratory of Hydraulic Engineering Safety and Simulation, Tianjin University. The physical flume is 35 m long and 7 m wide with a cylinder of 60 cm in diameter, as shown in Fig. 10 (a). The sediment bed is made of materials between 0.05 mm and 0.15 mm, with mean grain size  $D_{50} = 0.08$  mm and  $D_{75} = 0.12$  mm. The experimental cylinder is made of plexiglass, around which the high-resolution digital cameras are installed on the front, rear and lateral sides for real-time monitoring of the scouring process. This is shown in Fig. 10 (b).

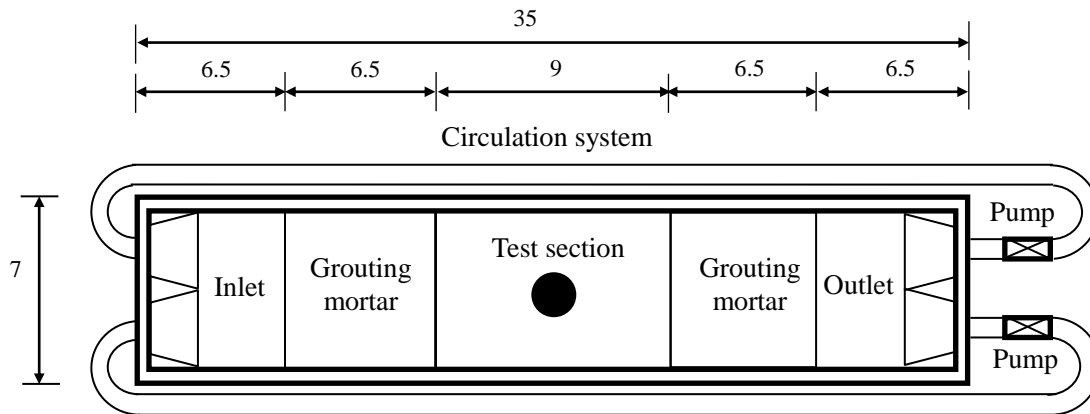


Fig. 10 (a) Laboratory flume for sediment bed scour around cylinder (unit: m)



Fig. 10 (b) Experimental cylinder and layout of inside cameras

The laboratory experiment has been strictly controlled under the condition of clear water scour, that is to say, the local scouring around the cylinder is exclusively due to the actions of horseshoe and lee-wake vortices without any influence from the upstream sediment movement. The experimental cylinder Reynolds number reaches nearly 100,000, therefore it is in the fully turbulent flow range.

It was disclosed in the experiment that at the early stage the scouring depth develops much faster on the lateral side of the cylinder, followed by more sediment movement on the front side. On the other hand, the sediment was deposited on the rear side at the beginning, due to the sediment materials scoured-off from the lateral and front sides of the cylinder. After this the local erosion process starts arising from the formation of lee-wake vortices. By analyzing the camera data, it shows that a higher flow velocity leads to a faster erosion rate as well as larger terminal scouring pit under the same flow depth. Accordingly, the timeline to reach the stable bed conditions becomes shorter. However, under the same frictional bed velocity, the present experiment found no obvious relationships between the flow depth and scouring depth, but rather the flow depth somewhat affects the scouring rate. Also the influence tends to be decreasing with an increase in the flow depth.

Two groups of the experimental study were carried out. In the first, three different flow depths were used as  $h = 30$  cm, 40 cm and 50 cm, respectively, while the bed frictional velocity was kept unchanged at  $u_* = 0.0156$  m/s  $\sim$  0.0158 m/s. In the second, the flow depth was fixed at  $h = 30$  cm, while different bed frictional velocities  $u_*$  were examined. Fig. 11 shows a contour map of the final stable scouring pit (where the unit is in meter) and corresponding experimental photo, for the flow condition of  $h = 0.3$  m and  $u_* = 0.0125$  m/s. It shows that under the unidirectional flow current, a scouring pit in the shape of inverse-cone is formed near the cylinder. The scouring depth on the upstream side is deeper than the downstream side, and there is a sediment deposition zone very close to the rear of cylinder along the centerline.

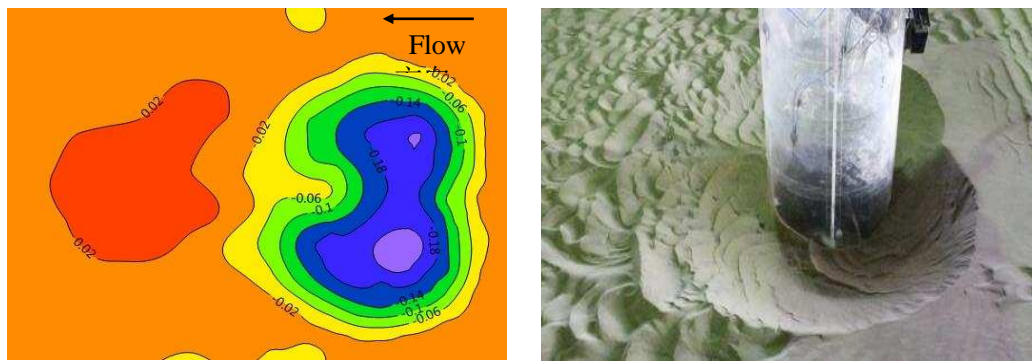


Fig. 11 Final sediment scouring pit for flow condition  $h = 0.3$  m and  $u_* = 0.0125$  m/s

With regard to the present experimental study, the pile Reynolds number ranged between 94200 and 129600. The sediment materials were naturally composed of and the grain diameters varied 0.05  $\sim$  0.15 mm, with  $d_{50} = 0.08$  mm and  $d_{75} = 0.12$  mm. In comparison, Roulund et al. (2005) adopted a Re number of 46000 with  $d_{50} = 0.26$  mm. Although non-cohesive sediments were used in both cases, the current sediment particles are more refined and more difficult to be initiated. So they need longer time to reach the equilibrium. For example, the dimensionless particle Re number is 0.0862  $\sim$  0.11793 in the present experiment, as compared with 1.075 in Roulund et al. (2005). Besides, the inflow process has been carefully controlled within the regime of the clear water scour and this provides valuable data for the validation of other numerical models as well. More details are found in Wang (2016).

## 5. ISPH Sediment Model Validation on Local Cylinder Scour

In this section the proposed 3D ISPH sediment erosion model is used to reproduce the previous laboratory experiment of flow passing through a cylinder over sediment bed.

### 5.1 Numerical setup and computational parameters

The numerical setup generally follows the layout of laboratory experiment so that a direct comparison can be made between the two and the experimental data can be used to validate the numerical results. In ISPH computation, the sediment mean diameter is 0.08 mm and the size of cylinder is 0.6 m, which are the same as those used in the experiment. Due to the concern of CPU load, the numerical flume has a shorter length and width than the experimental dimensions, i.e. the model flume is 5.2 m long (about 9 times of the cylinder diameter) and 4.5 m wide (about 7.5 times of the cylinder diameter). This setup could be justified by comparing the simulated transverse profiles of horizontal velocity  $U$  in the  $x$  direction at different locations away from the cylinder, as shown in Fig. 12. The velocities on the two side walls of the flume at the location of cylinder (indicated by 0 in the figure) are approximately 0.03 m/s larger than those at the location of 3D away from the cylinder.

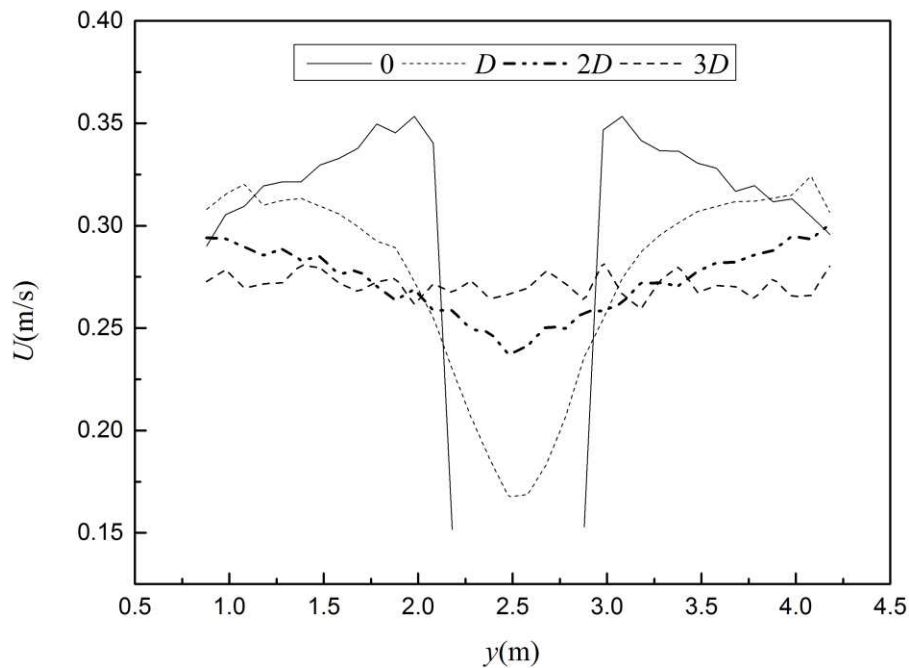


Fig. 12 Transverse profiles of ISPH simulated vertically-averaged horizontal velocity

The ISPH particle spacing is also used as 0.02 m, which is the same as that used in the fixed bed simulation. During the setup of interface and dummy boundary particles, the sediment bed of the region near the cylinder is placed with sufficient layers of the particles as potential candidate particles for the continuous erosion process. These particles, which are also future erodible sediment particles, are shown in red in Fig. 13 (a) and (b), respectively, as plan and side views, respectively, while the water particles are shown in blue. The left end side of the computational domain is the upstream boundary where a logarithmic inlet velocity profile is imposed, and the right end side is the downstream open boundary as specified in Wang et al. (2016).

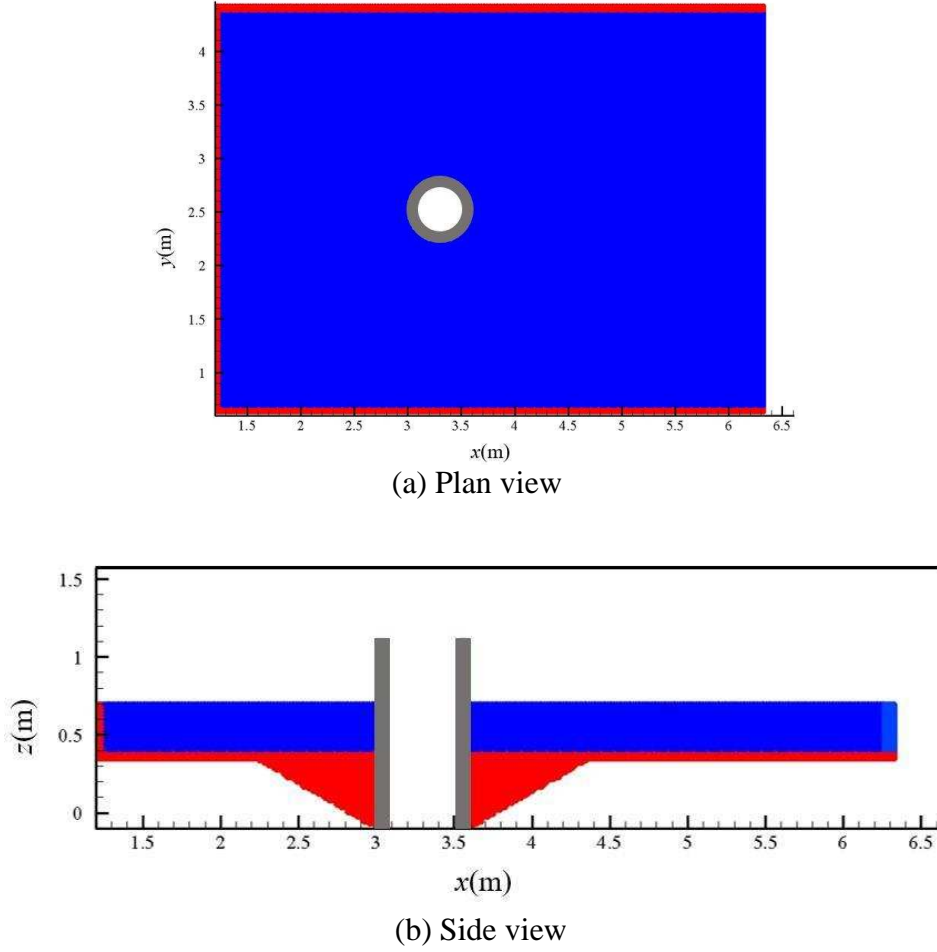


Fig. 13 Computational domain, including erodible bed particles (in red), non-erodible cylinder wall particles (in grey) and inner water particles (in blue)

As previously mentioned, the initial density of eroded sediment SPH particles, i.e. TWPs, is one of the most important parameters for the evaluations of bed scouring and sediment motion. Although this value can vary depending on the application cases, Sumer et al. (1996), among the others, found a threshold value of sediment volume concentration from the measurements on sand and plastic grains during the bed load transport, which stood at 30% at the very bottom of the movable grains and took a roughly linear profile within the bed layer. For the lower flow regime, the thickness of bed layer could be estimated as twice the sediment diameter (Wang et al., 2016). For the case of higher flow regime, the bottom sediments move in the mode of the sheet flows. Then the thickness of bed layer can be estimated by Wilson formula (1987).

As the size of SPH particle is generally much larger than the size of sediment grain, the initial density of turbidity water particle is calculated as the weighted average of sediment-water mixtures inside the bed layer and the dilute mixtures outside the bed layer, which is written as

$$\rho_{initial} = \frac{c_b \delta_b}{2} \rho_s + \left(1 - \frac{c_b \delta_b}{2}\right) \rho_w \quad (24)$$

where  $C_b$  denotes the mean volumetric fraction of the suspended solid phase inside the bed layer; and  $\rho_s$  and  $\rho_w$  the densities of sediment grain and water, respectively. Regarding the situation of present study, the thickness of bed layer was simply taken as 0.005 m by using the experiment results from Sumer et al. (1996). Considering the ISPH computational particle size 0.02 m, the initial sediment density of the TWPs can be calculated by

$$\begin{aligned}\rho_{initial} &= \frac{C_b}{2} * \frac{\delta_b}{D} * \rho_s + \left(1 - \frac{C_b}{2} * \frac{S}{D}\right) * \rho_w \\ &= 15\% * \frac{0.005}{0.02} * 2650 + \left(1 - \frac{0.005}{0.02} * 15\%\right) * 1000 \approx 1062 \text{ (kg/m}^3\text{)}\end{aligned}\quad (25)$$

For the present sediment bed, the threshold sediment initiation shear stress on a horizontal bed is calculated by using the standard Shield's formula as 0.18 N/m<sup>2</sup>. This value should be further corrected by considering the 3D scenarios of both longitudinal and transverse slope effects as represented by Eqs. (21) or (22), which are also related to the location of the particles. As a brief summary, the following key parameters are adopted in the computations: SPH particle size  $D = 0.02$  m, sediment grain diameter  $d_{50} = 0.08$  mm, maximum volumetric fraction  $C_b = 30\%$ , thickness of bed layer  $\delta_b = 0.005$  m, sediment density  $\rho_s = 2650$  kg/m<sup>3</sup>, sediment underwater repose angle  $\phi = 35^\circ$  and threshold sediment initiation shear stress on horizontal bed  $\tau_c = 0.18$  N/m<sup>2</sup>.

## 5.2 Model validations with experimental data

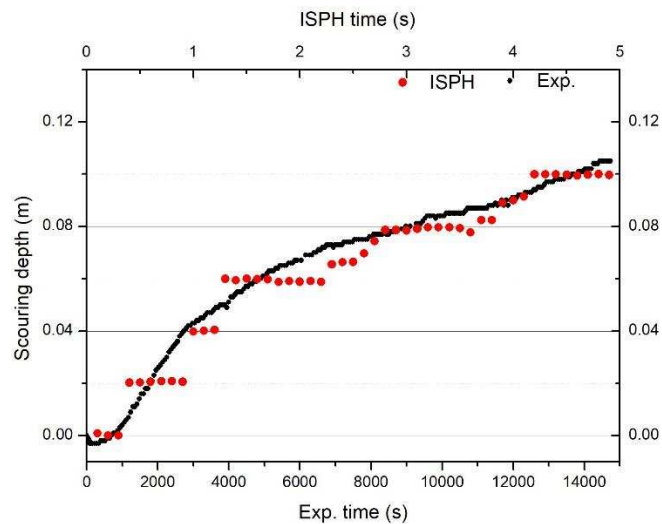
The 3D ISPH computed maximum scouring depth under five experimental conditions, as characterized by the different flow depths and frictional velocities, are shown in Table 1. It is found that the numerical results are generally consistent with the experimental data, although the former are around 4.9% ~ 25.6% higher than the latter. One reason on this discrepancy is that the bed coarsening effect was not considered in the numerical model, which should play an important role in the reduction of later scouring. In practice, this kind of conserved estimation is allowable for the safety of structures.

**Table 1. Experimental and ISPH maximum scouring depths**

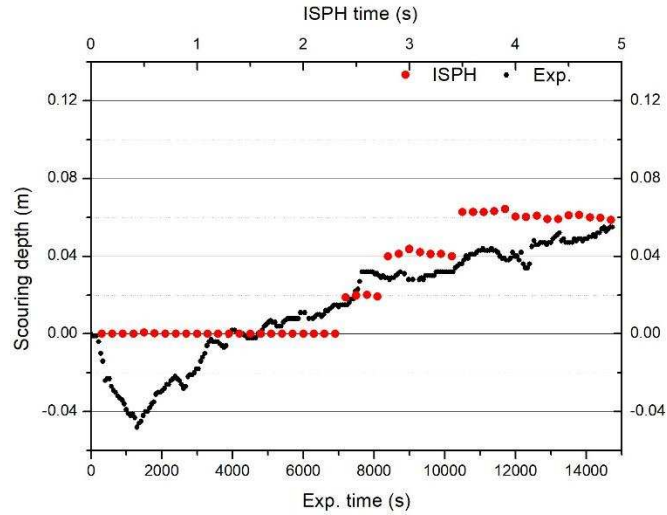
Exp no.	Flow depth (m)	Frictional velocity (m/s)	Exp scour depth (m)	ISPH scour depth (m)
1	0.3	0.013	0.191	0.240
2	0.3	0.016	0.285	0.299
3	0.3	0.017	0.360	0.395
4	0.4	0.016	0.293	0.341
5	0.5	0.016	0.304	0.345

For more in-depth model validations, the time-dependent scouring process is shown in

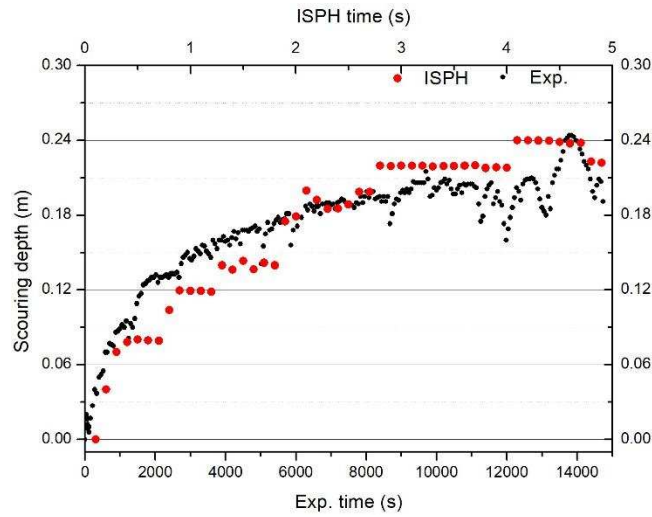
Fig. 14 (a) ~ (c), respectively, for the front, rear and lateral sides of the cylinder, between the experimental measurements and ISPH computational results. The results are presented for the experimental condition of flow depth  $h = 0.3$  m and frictional velocity  $u_* = 0.0125$  m/s. In ISPH computations, the maximum scouring depth was tracked by using the fluid particles closest to the interface wall boundary. Fig. 14 shows that the numerical results agree quite well with the experimental data during the erosion process (the step-like shape of the curve is due to the resolution of particle size). However, it should be noted that the timescale of experimental and numerical processes is much different. The reason on this mismatch has been explained in Wang et al. (2016). This is mainly due to the fact that the computational particle size is too large as compared with the individual sediment grain. In the ISPH erosion model, as long as the threshold condition is reached, the interface wall particles are instantly changed into the TWPs, which leads to substantial erosion of the sediment bed. A sensitivity study of using a smaller ISPH particle size has found to produce better timescale match between the model predictions and physical experiments. Therefore, it could be anticipated that if the SPH particle size is sufficiently small as close to the sediment grain scale, the numerical time pace should agree with the physical one. On the other hand, this also demonstrates the advantages of using the concept of turbidity water particle. TWP takes a different initial density as compared with the sediment grain density, and this can effectively reduce excessive bed scouring and save CPU expense. The use of real sediment grain density would lead to a more severe and unrealistic erosion process.



(a) Front side of cylinder



(b) Rear side of cylinder

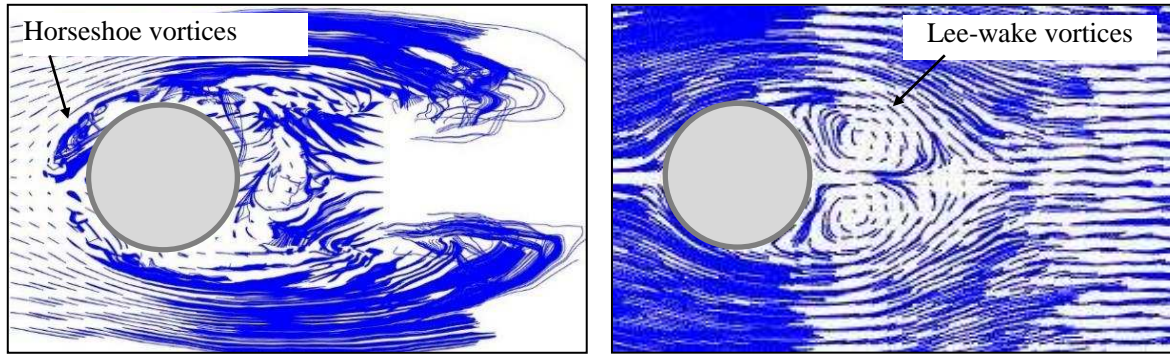


(c) Lateral side of cylinder

Fig. 14 Time-dependent scouring depth between experimental data and ISPH results

### 5.3 Results and discussions on horseshoe and lee-wakes vortices

As discussed before, the down-flows and horseshoe vortices in front of the cylinder, and the lee-wake vortices on the rear of the cylinder are the key hydrodynamic features demonstrated when the flow passing around. To illustrate this again, the ISPH computed flow streamlines are shown in Fig. 15 (a) and (b), respectively, for the front (near bed at  $z = 0.0 \sim 0.1$  m) and rear (near middle flow depth at  $z = 0.1 \sim 0.12$  m) sides of the cylinder. Besides, the time evolutions of computed vortices fields are shown in Fig. 16 for the near middle flow depth region at  $z = 0.1 \sim 0.12$  m. It is shown that the ISPH computations can well reproduce the frontal horseshoes and rear lee-wake vortices, thus provide realistic flow information for the sediment scouring predictions.



(a) Frontal horseshoe vortices ( $z = 0.0 \sim 0.1$  m) (b) Rear lee-wake vortices ( $z = 0.1 \sim 0.12$  m)

Fig. 15 ISPH computed streamlines

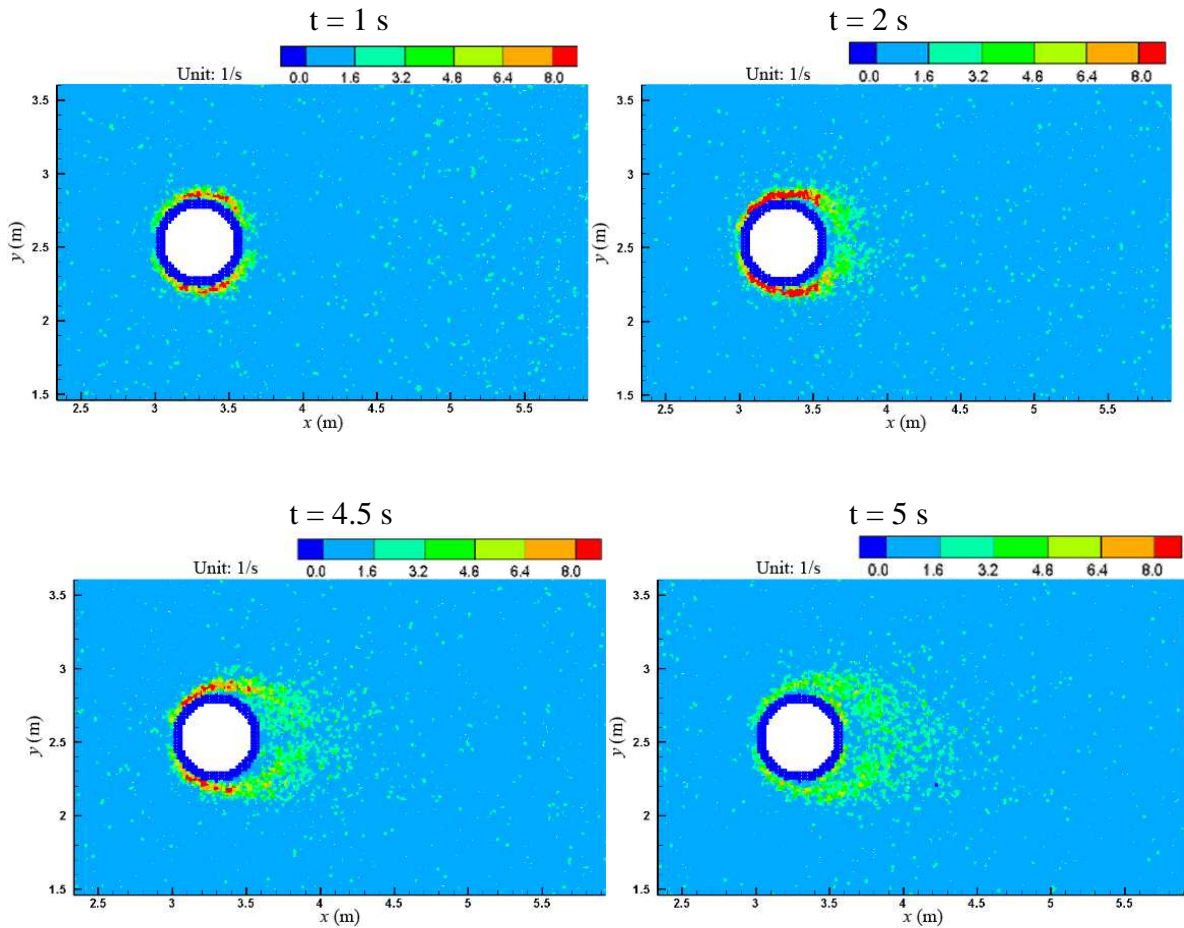
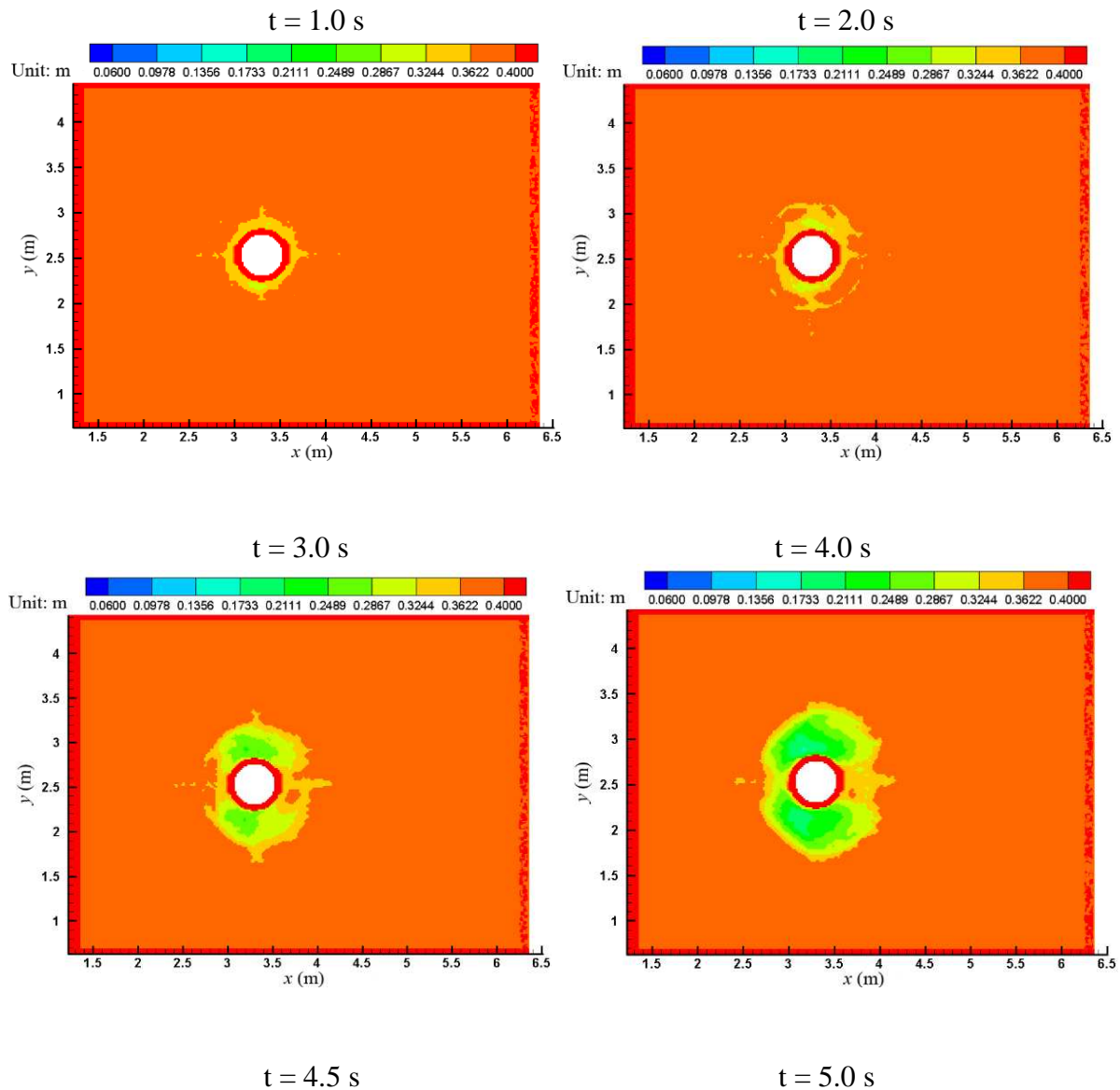


Fig. 16 ISPH computed time evolution of vortices fields for the near middle flow depth region at  $z = 0.1 \sim 0.12$  m

#### 5.4 Results and discussions on sediment bed erosion

From ISPH computations, Fig. 17 (a) gives the time series of bed erosion contours under

the experimental condition of flow depth  $h = 0.3$  m and frictional velocity  $u_* = 0.0125$  m/s. It shows that the proposed ISPH sediment model can realistically reproduce the local erosions when the flow passing around a cylinder. Due to the retardant effect from the cylinder, the down-flows generated on the front side and flows around the lateral sides of the cylinder increase with the flow depth in a relatively shallow water condition. As a result, the sediment within this area starts to move at the beginning of the scouring process. With the further development of scouring depth on the lateral sides, the scouring range also expands downstream gradually. The vortices generated near the bottom of the cylinder then enclose the structure to form frontal horseshoe vortices. Meanwhile, new vortices are continuously released from the lateral sides of the cylinder to constitute lee-wake vortices in the rear. The final bed erosion state, which is shown in the last sub-figure in Fig. 17 (a) at time  $t = 5.0$  s, is fairly similar to the corresponding experimental photo as shown in Fig. 17 (b) in terms of the shape of scour pit.



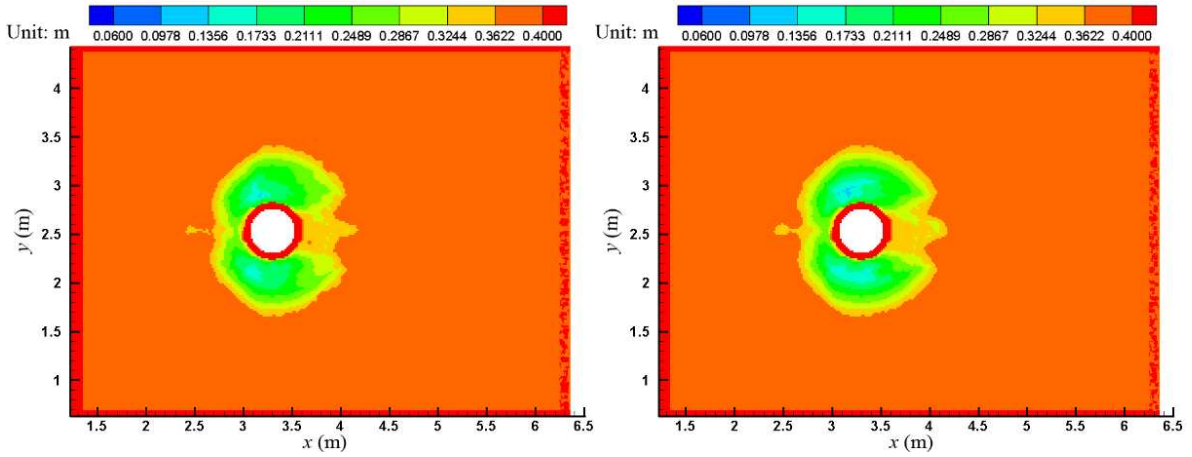
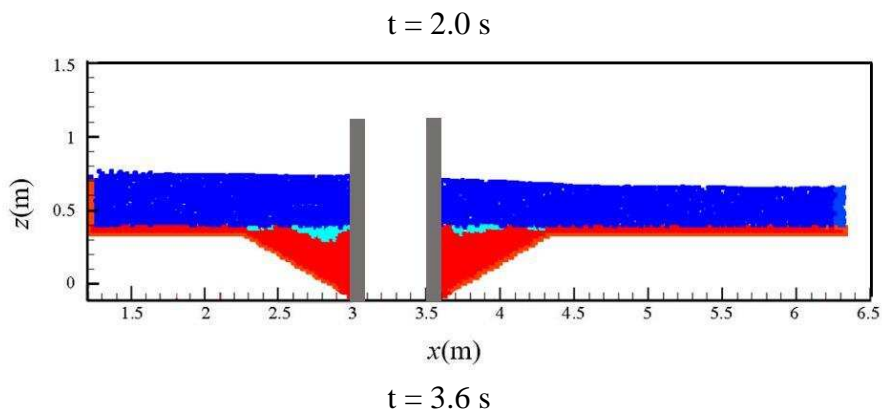


Fig. 17 (a) ISPH computed sediment bed scouring process



Fig. 17 (b) Experimental photo of final scouring pit

Fig. 18 shows the side view of scouring evolution time history, computed for the larger frictional velocity  $u_* = 0.0171$  m/s in the experimental case. Again the ISPH computations realistically reproduced the complex morphological process.



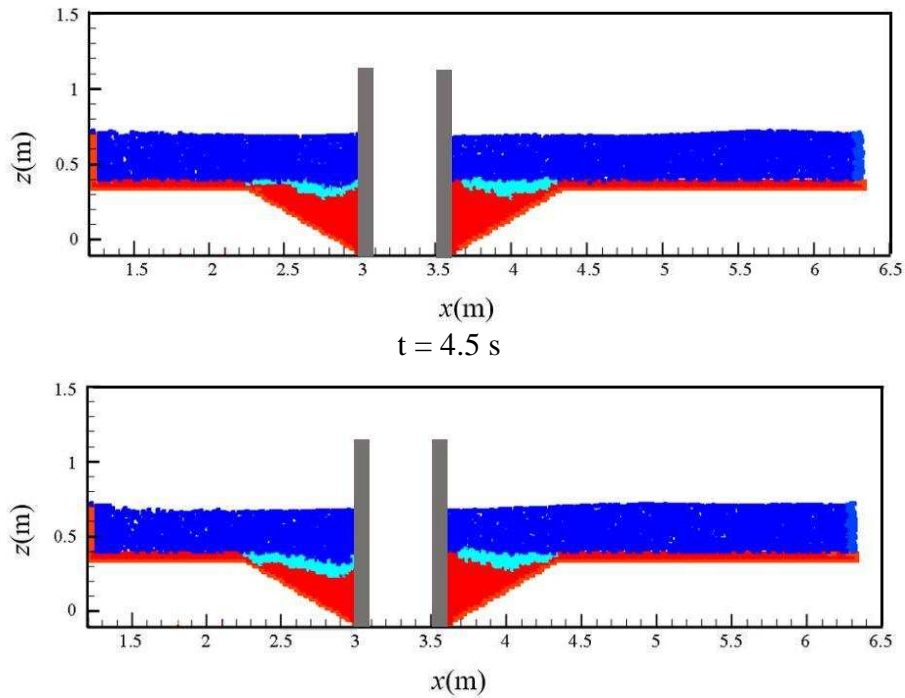


Fig. 18 Side view of ISPH computed sediment bed scouring process

### 5.5 Convergence study on numerical results

To check the convergence of model computations, an alternative particle size  $D = 0.012$  m was used, and the result was presented in Fig. 19 for the dynamic process of scouring depth on the rear side of the cylinder. It is clearly shown that the two SPH computational points are quite close to each other and also showed very similar tendency in the predictions. The good convergence behavior of the model is thus demonstrated.

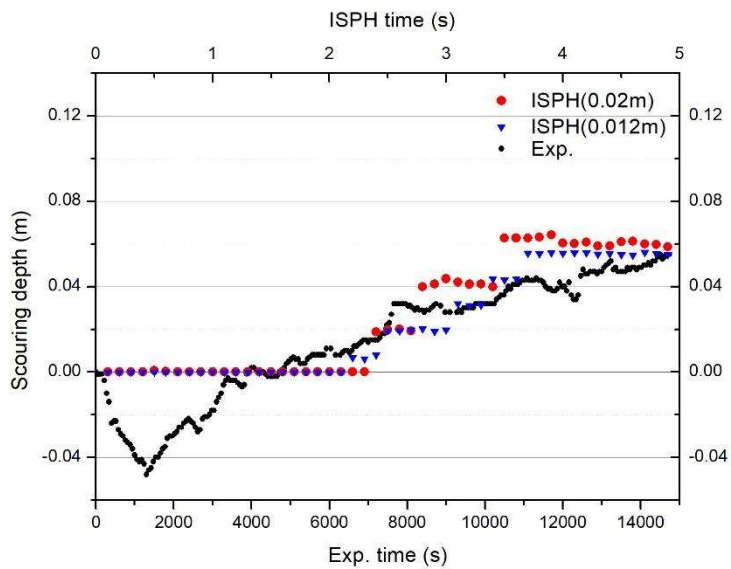
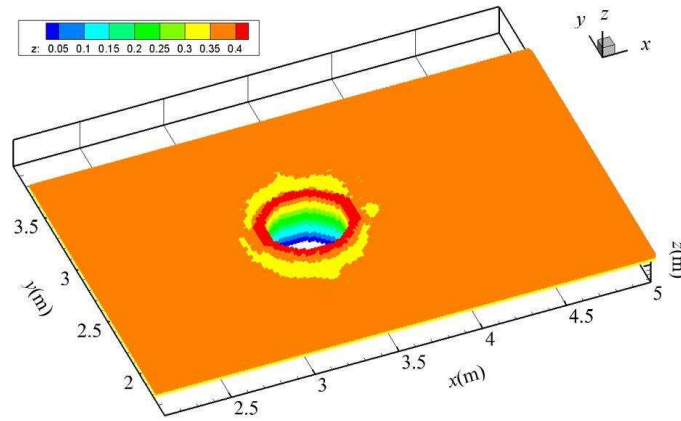


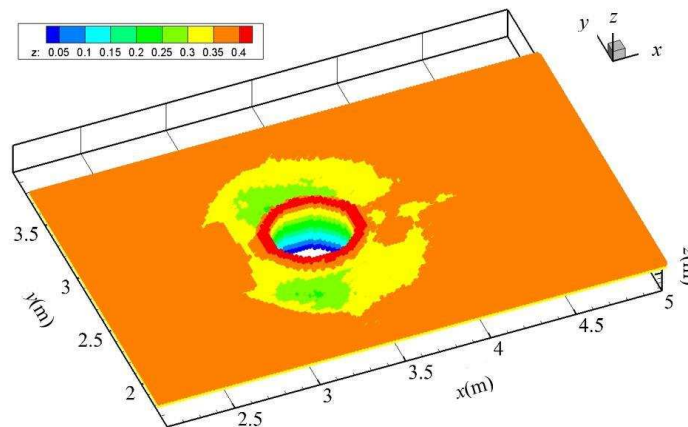
Fig. 19 Convergence test of the ISPH erosion model

### 5.6 3D scour development and bed shear stress distribution

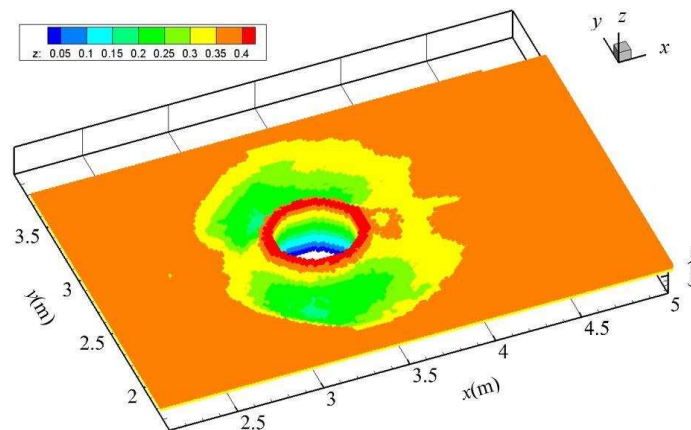
As a more robust illustration of the 3D ISPH modeling, the dynamic process of scour development of the sediment bed is shown in Fig. 20 (a) ~ (d), at time  $t = 2, 3, 4$  and  $5$  s, respectively. There is no experimental photo available for a comparison on the evolution but a final stable one has been shown in Fig. 17 (b).



(a)  $t = 2$  s



(b)  $t = 3$  s



(c)  $t = 4$  s

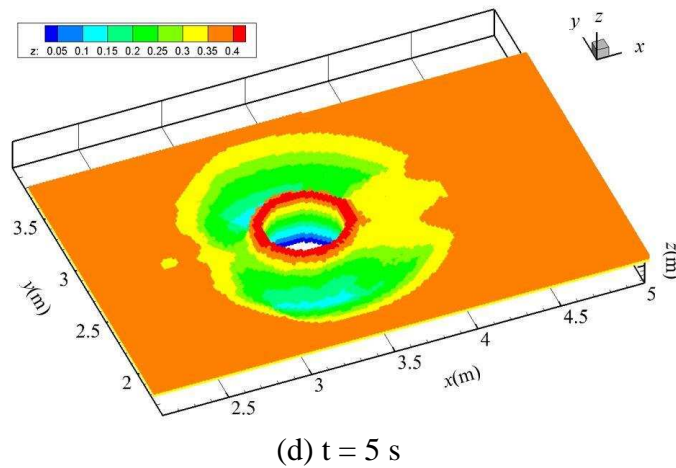
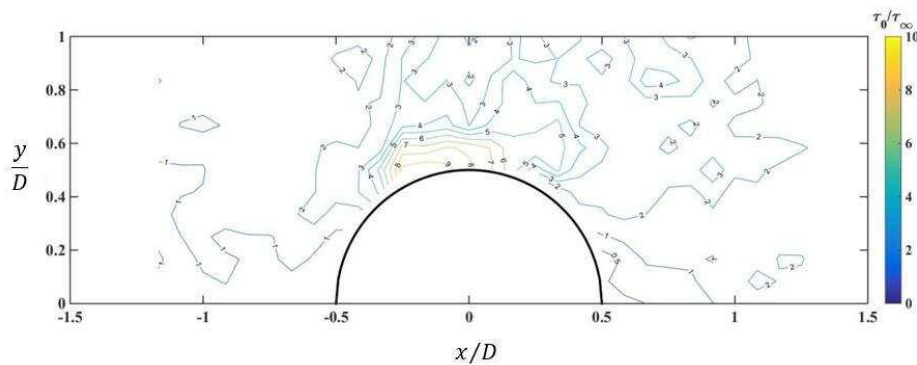
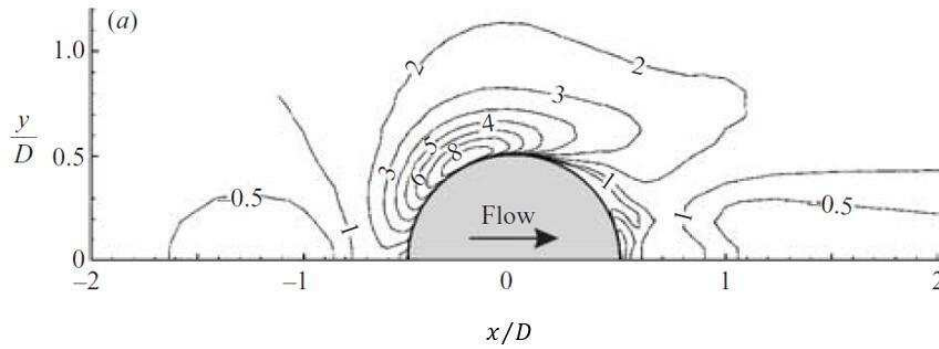


Fig. 20 3D representations of the scour development

Finally, the computed bed shear stress distributions under the steady flow state based on the assumption of fixed bed conditions are shown in Fig. 21 (a). Since there was no experimental data available for a direct comparison either, a qualitative comparison is thus made with the shear stress results from Roulund et al. (2005) in Fig. 21 (b). In spite of the differences in the flow and cylinder conditions, the normalized shear stresses near the cylinder from both results demonstrate very similar patterns. That is to say, the amplitude of the shear stress is generally similar to each other and also the maximum shear stress point is located somewhere near the lateral cylinder wall around  $45^\circ$  in the upstream direction in both ISPH's and Roulund et al.'s (2005). Although the ISPH shear stress contours are not very smooth due to the relatively rough particle size, the proposed model looks quite promising in that the main features of the shear stress field have been reasonably captured due to the use of the robust sub-particle-scale (SPS) turbulence model benchmarked by Gotoh et al. (2001), in view that not many SPH works demonstrated the accuracy of the shear stress calculations.



(a) ISPH shear stress



(b) Fig. 26 in Roulund et al. (2005)

Fig. 21 Comparisons of shear stress distributions near cylinder for a fixed bed

## 6. Conclusions

The paper proposed a fully 3D ISPH water-sediment erosion model for the local bed scouring when the unidirectional flow passes a vertical cylinder of relatively large size. One main feature of the sediment model is the use of the turbidity water particle (TWP) concept, for which the eroded SPH particles are treated as the water-sediment mixture and therefore they carry an initial density depending on the properties of the bed-load layer under low flow regime or sheet-flow layer under high flow regime, as well as the SPH particle size. The proposed ISPH algorithm implements the previous erosion model of Wang et al. (2016) that is based on the Shields' theory with additional corrections to account for the longitudinal and transverse sloping beds in order to extend this model to complex 3D applications. The model has been tested against the experimental results with both the fixed and mobile beds. In the latter case, valuable data on the time evolution of the clear-water scouring around a submerged cylinder in a unidirectional current have been collected in a dedicated laboratory experiment. The comparisons showed that the proposed ISPH model can simulate the relevant features of the flow (i.e. horseshoe and lee-wake vortices) as well as the dynamics of the induced scour with suitable degree of accuracy for the engineering purposes. Even if in some cases the percentage gap between the experimentally and numerically predicted scouring depth was significant, it could be noticed that the scouring process is actually affected by several random factors and therefore highly reliable predictions of the scouring effects are very difficult to obtain even with the experimental modelling. Generally speaking, the present ISPH erosion model should be able to provide useful information to the practical field with large diameter of the cylinder. All of the computations carried out in this paper demonstrated that CISP-HS-HL-ECS scheme (Gotoh et al., 2014) leads to an accurate ISPH

simulation in the flow field without any observed non-physical behaviours under the high Re numbers, in spite of the lack of extra particle stabilization techniques such as documented by Tsuruta et al. (2013) and Khayyer et al. (2017).

Furthermore, if following a probabilistic approach (Manenti et al., 2006), the proposed numerical model may also be used as an effective engineering tool for simulating the influence of stochastic factors related to both the sediment and flow characteristics on the prediction of the scour depth. Besides, the inclusion of sediment deposition mechanisms would significantly enhance the prediction capacity of the model in future applications.

## Acknowledgments

This research work has been financed by the National Natural Science Foundation of China (Grant No. 51779170 and 51379143) and Innovative Research Groups of the National Natural Science Foundation of China (Grant No. 51621092). We are also very grateful to Professor Philip Li-Fan Liu, Vice President of the National University of Singapore, for his constructive comments during the revision of the manuscript.

## Appendix

To calculate the angles such as  $\alpha$  and  $\beta$  in Fig. 1, the following procedures are carried out. Firstly by using the MLS approach, the normal vector of the plane, where a particle P is located, can be found by  $\mathbf{c} = (n_x, n_y, n_z)$ , as shown in Fig. A1. Note it has been defined that the x-axis of the local coordinate lies in the same vertical plane as that of the global one, so a full view of the global coordinate is also shown in Fig. A1, and the vector  $\mathbf{c}$  is projected to the different coordinate planes as l, m and n, respectively. Then the intersection lines between the local coordinate plane  $S'$  and global coordinate systems are obtained as o, w and q. The relationships are established as below:

$$\tan\beta = \frac{n_x}{n_z} \quad (\text{A1})$$

$$\tan\alpha = \frac{n_y}{n_z} \quad (\text{A2})$$

By assuming the velocity vector of particle P to be  $\mathbf{a}$ , under the global coordinate system, then under the local coordinate it takes the form of  $\mathbf{d} = \mathbf{a} - \mathbf{c}(\mathbf{a} \cdot \mathbf{c})$  and the orientation of its x-axis becomes  $\mathbf{b} = \left(1, 0, -\frac{n_x}{n_z}\right)$ . As a result, the following relation is further obtained

$$\cos\gamma = \frac{\mathbf{d} \cdot \mathbf{b}}{|\mathbf{d}| \cdot |\mathbf{b}|} \quad (\text{A3})$$

where  $\cos\gamma < 0$  indicates the upward direction of the slope, while  $\cos\gamma > 0$  the downward direction.

The angle variables in Eq. (22) can accordingly be calculated by

$$\sin\beta = \left| \frac{n_x}{\sqrt{n_x^2 + n_z^2}} \right|, \quad \cos\beta = \left| \frac{n_z}{\sqrt{n_x^2 + n_z^2}} \right|,$$

$$\sin\alpha = \left| \frac{n_y}{\sqrt{n_y^2+n_z^2}} \right|, \quad \cos\alpha = \left| \frac{n_z}{\sqrt{n_y^2+n_z^2}} \right|, \quad (\text{A4})$$

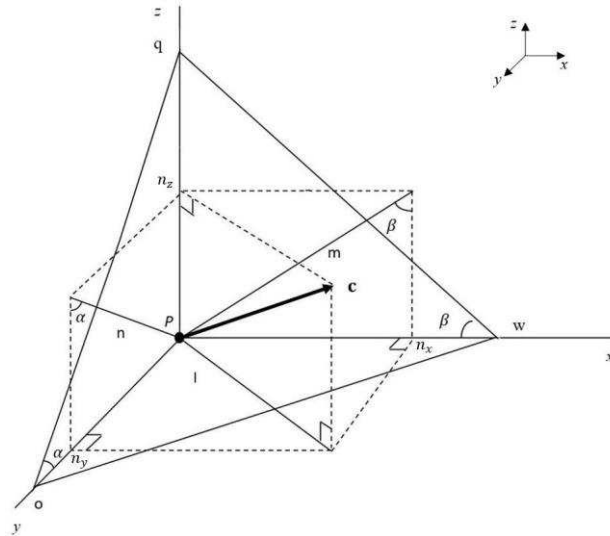


Fig. A1 The angle relationships between local and global coordinate systems

## References

Bouscasse, B., Colagrossi, A., Marrone, S. and Souto-Iglesias, A. (2017), SPH modelling of viscous flow past a circular cylinder interacting with a free surface, *Computers & Fluids*, 146, 190-212.

Dey, S. (2003), Threshold of sediment motion on combined transverse and longitudinal sloping beds, *Journal of Hydraulic Research*, 41(4): 405-415.

Dordoni, S., Malerba, P. G., Sgambi, L. and Manenti, S., Fuzzy reliability assessment of bridge piers in presence of scouring, *Proceedings of 5<sup>th</sup> International Conference on Bridge Maintenance, Safety and Management, Philadelphia, USA, 11-15 July 2010*, pp. 1388-1395.

Ellero, M. and Adams, N. A. (2011), SPH simulations of flow around a periodic array of cylinders confined in a channel, *International Journal for Numerical Methods in Engineering*, 86(8), 1027-1040.

Ettema, R., Kirkil, G. and Muste, M. (2006), Similitude of large-scale turbulence in experiments on local scour at cylinders, *Journal of Hydraulic Engineering*, 132, 33-40.

Fourtakas, G. and Rogers, B. D. (2016), Modelling multi-phase liquid-sediment scour and resuspension induced by rapid flows using Smoothed Particle Hydrodynamics (SPH) accelerated with a Graphics Processing Unit (GPU), *Advances in Water Resources*, 92, 186-199.

Fu, L. and Jin, Y. C. (2016), Improved multiphase Lagrangian method for simulating sediment transport in dam-break flows, *Journal of Hydraulic Engineering*, 142(6), 04016005.

- Gotoh, H., Khayyer, A., Ikari, H., Arikawa, T. and Shimosako, K. (2014), On enhancement of incompressible SPH method for simulation of violent sloshing flows, *Applied Ocean Res.*, 46, 104-115.
- Gotoh, H. and Sakai, T. (2006), Key issues in the particle method for computation of wave breaking, *Coast. Eng.*, 53(SI), 171-179.
- Gotoh, H., Shao, S. D. and Memita, T. (2004), SPH-LES model for numerical investigation of wave interaction with partially immersed breakwater, *Coastal Engineering Journal*, 46(1), 39-63.
- Gotoh, H., Shibahara, T. and Sakai, T. (2001), Sub-particle-scale turbulence model for the MPS method Lagrangian flow model for hydraulic engineering, *Comput. Fluid Dyn. J.*, 9(4), 339-347.
- Guandalini, R., Agate, G., Manenti, S., Sibilla, S. and Gallati, M., Innovative numerical modeling to investigate local scouring problems induced by fluvial structures, *Proceedings 6<sup>th</sup> International Conference on Bridge Maintenance, Safety and Management*, Stresa, Italy, 8-12 July 2012, pp. 3110-3116.
- Hayashi, M., Gotoh, H., Sakai, T. and Ikari, H. (2003), Lagrangian gridless model of toe scouring of seawall due to tsunami return flow, *Proc. of Asia and Pacific coast*, APAC, 1-12.
- Kazemi, E., Nichols, A., Tait, S. and Shao, S. D. (2017), SPH modelling of depth-limited turbulent open channel flows over rough boundaries, *International Journal for Numerical Methods in Fluids*, 83(1), 3-27.
- Khanpour, M., Zarrati, A. R., Kolandoozan, M., Shakibaenia, A. and Amirshahi, S. M. (2016), Mesh-free SPH modeling of sediment scouring and flushing, *Computers & Fluids*, 129, 67-78.
- Khayyer, A. and Gotoh, H. (2011), Enhancement of stability and accuracy of the moving particle semi-implicit method, *J. Comput. Phys.*, 230(8), 3093-3118.
- Khayyer, A., Gotoh, H. and Shimizu, Y. (2017a), Comparative study on accuracy and conservation properties of two particle regularization schemes and proposal of an optimized particle shifting scheme in ISPH context, *Journal of Computational Physics*, 332, 236-256.
- Khayyer, A., Gotoh, H., Shimizu, Y. and Gotoh, K. (2017b), On enhancement of energy conservation properties of projection-based particle methods, *European Journal of Mechanics - B/Fluids*, 66, 20-37.
- Manenti, S. and Cecconi, G., Evaluation of wave damage in urbanized lagoons, *Civil-Comp Proceedings CST 2006*, Las Palmas de Gran Canaria, Spain, 12-15 September 2006, V. 83.
- Manenti, S., Pierobon, E., Gallati, M., Sibilla, S., D'Alpaos, L., Macchi, E. and Todeschini, S. (2016), Vajont disaster: smoothed particle hydrodynamics modeling of the postevent 2D experiments, *Journal of Hydraulic Engineering*, 142(4), 05015007.

- Manenti, S., Sibilla, S., Gallati, M., Agate, G. and Guandalini, R. (2012), SPH simulation of sediment flushing induced by a rapid water flow, *J. Hydraul. Eng., ASCE*, 138(3), 272-284.
- Marrone, S., Colagrossi, A., Antuono, M., Colicchio, G. and Graziani, G. (2013), An accurate SPH modeling of viscous flows around bodies at low and moderate Reynolds numbers, *Journal of Computational Physics*, 245, 456-475.
- Monaghan, J. J. (1992), Smoothed particle hydrodynamics, *Annu. Rev. Astronomy and Astrophysics*, 30, 543-574.
- Morris, J. P., Fox, P. J. and Zhu, Y. (1997), Modeling low Reynolds number incompressible flows using SPH, *Journal of Computational Physics*, 136(1), 214-226.
- Nestor, R. M. and Quinlan, N. J. (2013), Application of the meshless finite volume particle method to flow-induced motion of a rigid body, *Computers & Fluids*, 88, 386-399.
- Olsen, N. R. B. and Kjekkesvig, H. M. (1998), Three-dimensional numerical flow modeling for estimation of maximum local scour depth, *Journal of Hydraulic Research*, 36(4), 579-590.
- Olsen, N. R. B. and Melaaen, M. C. (1993), Three-dimensional calculation of scour around cylinders, *Journal of Hydraulic Engineering*, 119, 1048-1054.
- Omidvar, P., Stansby, P. K. and Rogers, B. D. (2012), Wave body interaction in 2D using smoothed particle hydrodynamics (SPH) with variable particle mass, *International Journal for Numerical Methods in Fluids*, 68(6), 686-705.
- Pahar, G. and Dhar, A. (2017), Coupled incompressible Smoothed Particle Hydrodynamics model for continuum-based modelling sediment transport, *Advances in Water Resources*, 102, 84-98.
- Petrini, F., Manenti, S., Gkoumas, K. and Bontempi, F. (2010), Structural design and analysis of offshore wind turbines from a system point of view, *Wind Engineering*, 34, 85-108.
- Ran, Q. H., Tong, J., Shao, S. D., Fu, X. D. and Xu, Y. P. (2015), Incompressible SPH scour model for movable bed dam break flows, *Advances in Water Resources*, 82, 39-50.
- Richardson, J. E. and Panchan, V. G. (1998), Three-dimensional simulation of scour-inducing flow at bridge piers, *Journal of Hydraulic Engineering*, 124, 530-540.
- Roulund, A., Sumer, B. M., Fredsøe, J. and Michelsen, J. (2005), Numerical and experimental investigation of flow and scour around a circular pile, *J. Fluid Mech.*, 534, 351-401.
- Shakibaenia, A. and Jin, Y. C. (2011), A mesh-free particle model for simulation of mobile-bed dam break, *Adv. in Water Res.*, 34(6), 794-807.

- Shao, S. D. and Lo, E. Y. M. (2003), Incompressible SPH method for simulating Newtonian and Non-Newtonian flows with a free surface, *Advances in Water Resources*, 26(7), 787–800.
- Sheppard, D. M., Odeh, M. and Glasser, T. (2004), Large scale clear-water local pier scour experiments, *Journal of Hydraulic Engineering*, 130, 957-963.
- Soulsby, R. L. and Damgaard, J. S. (2005), Bedload sediment transport in coastal waters, *Coastal Eng.*, 52 (8), 673-689.
- Sumer, B. M. and Fredsøe, J. (2001), Scour around vertical pile in combined wave and current, *Journal of Hydraulic Engineering*, 127, 403-411.
- Sumer, B. M., Kozkiewicz, A., Fredsoe, J. and Deigaard, R. (1996), Velocity and concentration profiles in sheet-flow layer of movable bed, *Journal of Hydraulic Engineering*, 122(10), 549-558.
- Tsuruta, N., Khayyer, A. and Gotoh, H. (2013), A short note on dynamic stabilization of moving particle semi-implicit method, *Computers & Fluids*, 82, 158-164.
- Wang, D. (2016), ISPH Simulation and Experimental Research of Local Scour around Structures under Currents, PhD thesis, Tianjin University, China (in Chinese).
- Wang, D., Li, S. W., Arikawa, T. and Gen, H. Y. (2016), ISPH simulation of scour behind seawall due to continuous tsunami overflow, *Coastal Engineering Journal*, 58(3), 1650014.
- Wen, H. J., Ren, B., Dong, P. and Wang, Y. X. (2016), A SPH numerical wave basin for modeling wave-structure interactions, *Applied Ocean Research*, 59, 366-377.
- Wilson, K. C. (1987), Analyses of bed-load motion at high shear stress, *Journal of Hydraulic Engineering*, ASCE, 113(1), 97-103.
- Xu, H. and Lin, P. (2017), A new two-step projection method in an ISPH model for free surface flow computations, *Coast. Eng.*, 127, 68-79.
- Yildiz, M., Rook, R. A. and Suleman, A. (2009), SPH with the multiple boundary tangent method, *International Journal for Numerical Methods in Engineering*, 77(10), 1416-1438.
- Zanganeh, M., Yeganeh-Bakhtiary, A. and Abd Wahab, A. K. (2012), Lagrangian coupling two-phase flow model to simulate current-induced scour beneath marine pipelines, *Applied Ocean Research*, 38, 64-73.
- Zheng, X., Shao, S., Khayyer, A., Duan, W., Ma, Q. and Liao, K. (2017), Corrected first-order derivative ISPH in water wave simulations, *Coastal Engineering Journal*, 59, 1750010.

